Jagiellonian University in Krakow
Faculty of Physics, Astronomy and Applied Computer Science
Department of Experimental Particle Physics and Its Applications

Anna Giebułtowska
Student ID: 1203064

Impact of positron range on image reconstruction in ^{18}F and ^{44}Sc PET imaging.

Wpływ zasięgu pozytonów na rekonstrukcję obrazu w badaniach PET z użyciem ^{18}F i ^{44}Sc

Bachelor Thesis
in the field of Biophysics

Thesis supervisor:
dr Szymon Niedźwiecki
Department of Experimental
Particle Physics and Its Applications

Krakow 2026

Author's Statement

Aware of legal responsibility, I declare that this diploma thesis has been written by me independently and does not contain content obtained in a manner inconsistent with applicable regulations. I also declare that the presented work has not been previously the subject of procedures related to obtaining a professional title at a higher education institution.

Krakow, date ....

(Author's signature)

Supervisor's Statement

I confirm that this thesis has been prepared under my supervision and qualifies for presentation in the procedure for awarding a professional title.

Krakow, date ....

(Supervisor's signature)

Abstract

Positron range represents a fundamental physical limit to spatial resolution in positron emission tomography (PET). While this effect is generally negligible for standard isotopes such as ^{18}F, radionuclides with higher positron emission energies, i.e. ^{44}Sc, can introduce noticeable image blurring. This study investigates the impact of positron range on PET image quality by evaluating and comparing simulated and experimental data for both ^{18}F and ^{44}Sc.

For this work a custom Monte Carlo simulation was developed, incorporating two analytical models for positron range - the maximum and mean range. Using this framework, spheres of a standard NEMA IQ phantom were modeled in a water medium with each isotope to generate activity distributions. Sphere diamateres were estimated across three intesity thresholds: 40%, 50%, and 80%.

The simulation results showed that applying the maximum range model allowed for an accurate reconstruction of the 37 mm sphere for ^{18}F at the 50% threshold (37.58 $\pm$ 2.08 mm), whereas the same conditions yielded slightly reduced dimensions for ^{44}Sc (36.56 $\pm$ 1.94 mm). Conversely, the mean range model produced systematically smaller diameters with significantly higher uncertainties for both isotopes. Analysis revealed a clear spill-out effect for ^{44}Sc, reaching up to 14.5% in the 10 mm sphere, compared to less than 0.2% for ^{18}F.

Experimental measurements performed with the Modular J-PET scanner confirmed a substantial overestimation of the ^{44}Sc sphere diameters at the 40% threshold (33.33 $\pm$ 5.73 mm for the 22 mm sphere), while the ^{18}F measurements aligned with established literature values. Although the simulations successfully reproduced the qualitative differences between the two isotopes, they tended to underestimate the overall magnitude of the positron range effect, which is consistent with independent findings using PHITS simulations.

Presented results confirm that the positron range of ^{44}Sc affects PET image reconstruction and must be considered for accurate clinical imaging. Furthermore, the applied Monte Carlo method offers a practical, computationally efficient approach for the initial estimation of these blurring effects, despite its inherent simplifications.

Streszczenie

Zasięg pozytonów stanowi fundamentalne fizyczne ograniczenie rozdzielczości w pozytonowej tomografii emisyjnej (PET). Choć efekt ten jest na ogół pomijalny dla standardowych izotopów, takich jak ^{18}F, radionuklidy o wyższych energiach emisji pozytonów, takie jak ^{44}Sc, mogą wprowadzać zauważalne rozmycie obrazu. W niniejszej pracy zbadano wpływ zasięgu pozytonów na jakość obrazu PET poprzez analizę i porównanie danych symulacyjnych oraz eksperymentalnych dla ^{18}F i ^{44}Sc.

Na potrzeby tych badań opracowano autorską symulację Monte Carlo, uwzględniającą dwa analityczne modele zasięgu pozytonów - zasięg maksymalny i średni. Wykorzystując to środowisko, w ośrodku wodnym zamodelowano kule standardowego fantomu NEMA IQ dla każdego z izotopów, aby wygenerować rozkłady aktywności. Następnie zrekonstruowano te rozkłady, a uzyskane średnice kul zmierzono na trzech progach intensywności (40%, 50% i 80%).

Wyniki symulacji wykazały, że zastosowanie modelu maksymalnego zasięgu pozwoliło na dokładną rekonstrukcję kuli o średnicy 37 mm dla ^{18}F przy progu 50% (37,58 ± 2,08 mm), podczas gdy w tych samych warunkach dla ^{44}Sc uzyskano nieznacznie zaniżone wymiary (36,56 ± 1,94 mm). Z kolei model średniego zasięgu dał systematycznie mniejsze średnice przy znacznie wyższych niepewnościach dla obu izotopów. Analiza rozkładów punktów zatrzymania wykazała wyraźny efekt ucieczki aktywności (spill-out) dla ^{44}Sc, sięgający 14,5% w kuli o średnicy 10 mm, w porównaniu do poniżej 0,2% dla ^{18}F.

Pomiary eksperymentalne przeprowadzone przy użyciu skanera Modular J-PET pokazały przeszacowanie średnicy kul dla ^{44}Sc przy progu 40% (33,33 ± 5,73 mm dla kuli 22 mm), podczas gdy wyniki pomiarów dla ^{18}F były zgodne z ustalonymi wartościami literaturowymi. Mimo że symulacje poprawnie odtworzyły jakościowe różnice między oboma izotopami, wykazywały tendencję do niedoszacowywania całkowitej wielkości wpływu zasięgu pozytonów, co jest zgodne z niezależnymi wynikami uzyskanymi za pomocą symulacji PHITS.

Otrzymane wyniki potwierdzają, że zasięg pozytonów ^{44}Sc wpływa na rekonstrukcję obrazu PET i musi być brany pod uwagę w celu zapewnienia dokładnego obrazowania klinicznego. Ponadto zastosowana metoda Monte Carlo, pomimo swoich wrodzonych uproszczeń, oferuje praktyczne i wydajne obliczeniowo podejście do wstępnego szacowania tych efektów rozmycia.

Acknowledgements

I would like to express my sincere gratitude to my supervisor for his guidance and valuable advice, without whom I would not have been able to finish writing my thesis. I am thankful for the opportunity to write this paper as part of the Department of Experimental Particle Physics and Its Applications under the leadership of Prof. Paweł Moskal . I would also like to thank Dr. Martin Readler for creating the code that transformed raw experimental data in .img files into the NIfTI format used in my work. The data were kindly shared with me by mgr. Manish Das, whom I would like to thank. Finally, I would like to express my gratitude to my boyfriend Michał Miziołek for helping me with coding in Python and giving me strength throughout the year to write this thesis.

This work was supported in part by the National Science Centre of Poland under Grant MAESTRO 2021/42/A/ST2/00423 (P.M.), Grant OPUS 2021/43/B/ST2/02150 (P.M.), Grant OPUS24+LAP Grant 2022/47/I/NZ7/03112 (E.S.), Grant SONATA 2023/50/E/ST2/00574 (S.S.), and Grant SONATA 2020/38/E/ST2/00112 (E.P. del R.); in part by the Ministry of Science and Higher Education under Grant IAL/SP/596235/2023 (P.M.); in part by the SciMat and qLife Priority Research Areas Budget under the Program Excellence Initiative - Research University at Jagiellonian University (P.M. and E.S.); in part by the Research Support Module as part of the Excellence Initiative - Research University Program at Jagiellonian University (M.D.); and in part by the Polish High-Performance Computing Infrastructure PLGrid (HPC Center: ACK Cyfronet AGH) for providing Computer Facilities and support within Computational Grant PLG/2024/017688.

Contents

List of Abbreviations

PET Positron Emission Tomography

J-PET Jagiellonian Positron Emission Tomograph

Ps Positronium

o-Ps ortho-Positronium

p-Ps para-Positronium

LOR Line of Response

PM photomultiplier

PMT photomultiplier tube

MC Monte Carlo

NEMA National Electrical Manufacturers Association

PSF Point Spread Function

PHITS Particle and Heavy Ion Transport code System

PENELOPE PENEtration LOss of Positive Electrons (program for Monte Carlo simulation of particle transport)

GEANT-4 GEometry ANd Tracking (toolkit for simulation of particle passage through matter)

NIfTI Neuroimaging Informatics Technology Initiative (file format for neuroimaging data)

FWHM Full Width at Half Maximum

AFOV Axial Field of View

CT Computed Tomography

MRI Magnetic Resonance Imaging

FDG Fluorodeoxyglucose

TOT Time Over Threshold

CRT Coincidence Resolving Time

PLI	Positronium Lifetime Imaging
CTW	Coincidence Time Window
DTW	Delayed Time Window

1 Introduction

1.1 Motivation

Positron Emission Tomography is an imaging method providing unparalleled information regarding the metabolism of malignancies inside the human body, especially useful in oncology for investigating tumor sizes and properties. Since it is such a useful technique, it is gaining popularity in hospitals and more research is being conducted into new radioisotopes suitable for use during the imaging procedure.

Current PET scanners can be divided into three categories based on the axial field of view (AFOV): dedicated organ scanners, whole-body scanners with an AFOV of 16–26 cm, and total-body scanners such as the uEXPLORER system with an AFOV of 194 cm. The total-body design provides a sensitivity gain of 10 to 40 times over conventional systems, enabling lower administered activity, faster scans, or improved image quality. A similar total-body coverage at a reduced cost is proposed by the J-PET concept, which replaces inorganic crystals with plastic scintillator strips, offering a projected sensitivity gain of approximately 13 to 38 times [1, 2].

However, like every other imaging method, PET has a limit to its spatial resolution, with the best modern tomographs achieving reconstructions of structures as small as approximately 1.5 mm for dedicated brain scanners and around 2.5-3 mm for whole-body clinical systems [3, 4].

Spatial resolution is a parameter describing the smallest objects that can be distinguished with a PET scanner. Historically, efforts to improve spatial resolution have focused on detector properties and reconstruction algorithms. More recently, a new factor influencing spatial resolution has been taken into account. Positrons emitted from radioisotopes travel a finite distance within the tissue, and the point they reach before annihilation is a function of the positron energy and the density of the material the particle travels through. Consequently, radioisotopes with higher emission energies, which produce a broader energy spectrum of emitted positrons, have a negative impact on spatial resolution [5]. Despite this, the radioisotope chosen for the imaging procedure is not yet routinely accounted for during the image reconstruction phase [6].

Accordingly, a niche within PET research has opened: first, to identify commonly used and emerging radioisotopes, whose impact on spatial resolution through positron range is measurable, rather than being lost in detector and reconstruction effects. Secondly, it is important to quantify the influence of positron range on image reconstruction, in order to eventually develop and implement correction algorithms during the reconstruction phase.

Such a correction would enable the detection of smaller pathological changes, such as early metastatic tumors, thereby improving diagnostic sensitivity.

In this work the impact of positron range of ^{18}F and ^{44}Sc on image reconstruction was investigated. Data for the estimation were obtained from experiment, and simulated using in-house developed Monte Carlo Simulation, employing two approaches - the maximum range and the mean range.

The impact of positron range for these two radioisotopes was determined qualitatively, by comparing the real diameters from NEMA IQ phantom (which was deployed during the experiment and simulated in Monte Carlo) spheres, with the diameters obtained from reconstructed images.

The results obtained during the analysis revealed that ^{44}Sc, being the higher-energy radioisotope, is more prone to limit spatial resolution, as its emitted positrons travel further from the emission site before annihilation compared to ^{18}F. The results also showed that the simulation underestimates the influence of positron range on image reconstruction, which is consistent with the state-of-the-art literature.

The work has six chapters and is structured as follows. Section History and principles of PET provides an overview of the principles underlying PET imaging. The concept of positron range is introduced in Section 2.4, and an overview of relevant radioisotopes is presented in Section 2.3. The experimental data acquisition is described in Section 3.1, with the Monte Carlo simulation method detailed in Section 3.2. The procedure for determining the apparent diameters is explained in Section 3.3. The results of the analysis are presented in Section 4.2 and discussed in Chapter Discussion of the Results.

1.2 Aim

The aim of this work is to investigate whether the positron range has a measurable impact on image reconstruction in PET for two radioisotopes: ^{18}F and ^{44}Sc. Since ^{44}Sc emits positrons with considerably higher energy than ^{18}F, the range of these positrons before annihilation is expected to be larger, which may lead to a degradation of the reconstructed image quality. Exploring this effect is particularly relevant in the context of the growing interest in ^{44}Sc as a PET imaging isotope for theranostic applications. For this investigation, both experimental data shared with the author of this work, and data obtained from a Monte Carlo simulation will be analysed, using the NEMA IQ phantom geometry as the common reference.

The NEMA IQ phantom is well suited for this purpose, as it contains six fillable spheres of known inner diameters (10, 13, 17, 22, 28, and 37 mm) embedded in a cylindrical background volume, see Fig. 1.1. This design allows for a direct comparison between the real sphere dimensions and the diameters reconstructed from the PET data at varying intensity thresholds. By evaluating the recovered sphere sizes as a function of the chosen threshold, the extent to which positron range biases the reconstructed geometry can be assessed.

Figure 1.1: NEMA Image Quality phantom used in the experimental evaluation. The phantom contains six fillable spheres of varying diameters (10, 13, 17, 22, 28, and 37 mm) mounted on a central rod within an elliptical water-filled chamber, allowing assessment of image quality and spatial resolution under standardized conditions. Figure adapted from [7].

Specifically, this work will compare the experimental and simulated sphere diameters obtained for ^{44}Sc and ^{18}F at selected intensity thresholds, examine the dependence of the reconstructed diameter on the threshold choice, and evaluate whether the two analytical positron range models employed in the simulation (the maximum range and the mean range) reproduce the experimentally observed differences between the isotopes. The results will indicate whether a correction for positron range effects should be considered in the reconstruction phase for higher-energy positron emitters such as ^{44}Sc.

The Monte Carlo simulation of positron ranges in the NEMA IQ phantom geometry, the program for the determination of sphere diameters from reconstructed images, as well as all subsequent estimations and data analysis presented in this work were developed and performed by the author of this thesis.

2 Positron Emission Tomography

2.1 History and principles of PET

The rapid development in particle physics during the twentieth century culminated in the creation of the first clinical positron imaging device in 1953 by Gordon Brownell and William Sweet [8]. Originally designed for the localization of brain tumors, this device laid the groundwork for modern medical imaging. However, the theoretical foundations of this technology go back as far as 1928, when Paul Dirac combined quantum mechanics and special relativity to predict the existence of the positron. This was subsequently confirmed by Carl D. Anderson's experimental observation of the "anti-electron" in a cloud chamber in 1932 [9]. The profound question remains: how did the fundamental discovery of an antiparticle lead to what is now considered "the most specific and sensitive means for imaging molecular interactions and pathways within the human body" [8]?

The clinical value of PET lies in its ability to visualise metabolic and molecular processes in vivo, rather than merely depicting anatomical structure. Unlike methods such as computed tomography (CT) or magnetic resonance imaging (MRI), which excel at providing high-resolution morphological information, PET offers insight into the physiological behaviour of tissues. The most widely used radiotracer, ^{18}F-fluorodeoxyglucose (FDG), exploits the elevated glucose metabolism characteristic of most malignant cells, enabling PET to distinguish between metabolically active tumour tissue and surrounding healthy structures with high sensitivity and specificity. This capability has made FDG-PET, and subsequently FDG-PET/CT, a standard tool in oncology for tumour staging, restaging, assessment of treatment response, and radiotherapy planning. A key advantage of PET over conventional imaging is its ability to detect metabolic changes at an early stage of therapy, well before tumour shrinkage becomes apparent on CT or MRI. Studies have shown that changes in glucose metabolism can be identified within days of initiating treatment, providing clinicians with an early indicator of chemosensitivity. In the management of lymphoma, FDG-PET/CT has proven more sensitive than contrast-enhanced CT for staging, leading to an upgrade in disease stage and a subsequent change in treatment strategy in approximately 10-15% of patients [10].

Beyond oncology, PET has found applications in neurology, cardiology, and an expanding range of research fields. It is considered the most sensitive noninvasive technique available for studying physiology, metabolism, and molecular pathways in the human body [11]. Recent developments in total-body PET scanners, which provide up to a 40-fold increase in geometric sensitivity compared to conventional systems, have opened new possibilities for low-dose imaging, dynamic studies of tracer kinetics, and simultaneous multi-organ assessment [11]. These advances extend the reach of PET into areas such as toxicology, drug development, monitoring of cellular and nanoparticle-based therapies, and maternal-fetal medicine, where the ability to track molecular processes with high sensitivity is of particular value.

When a positron is emitted into surrounding tissue, it first undergoes thermalization, losing its kinetic energy through inelastic collisions with electrons. The finite distance the positron travels before annihilation — known as the positron range — depends on its initial kinetic energy and the density of the surrounding tissue; for ^{18}F, this range is approximately 1 mm in tissue, and it represents a fundamental physical limit on the spatial resolution of PET imaging [8]. Once it reaches near-thermal energies, its interaction with an electron, results most commonly in the direct annihilation. To conserve both energy and momentum, this process typically yields two collinearly emitted gamma rays (at an angle of approximately 180 degrees), each carrying an energy of 511 keV in accordance with Einstein's mass-energy equivalence, $E = mc^2$. While the two-photon emission is the dominant mechanism, other annihilation modalities exist with much lower probabilities, such as three-gamma-ray, radiationless, and single-quantum annihilations. Furthermore, a positron and an electron can temporarily form a quasi-stable, hydrogen-like neutral bound state known as positronium (Ps) [12]. Positronium primarily exists in one of two ground states: the short-lived, singlet para-positronium (p-Ps) or the longer-lived, triplet ortho-positronium (o-Ps), the study of which remains highly relevant to advanced diagnostic applications, with first imaging utilizing the o-Ps performed in Jagiellonian University in Cracow [13].

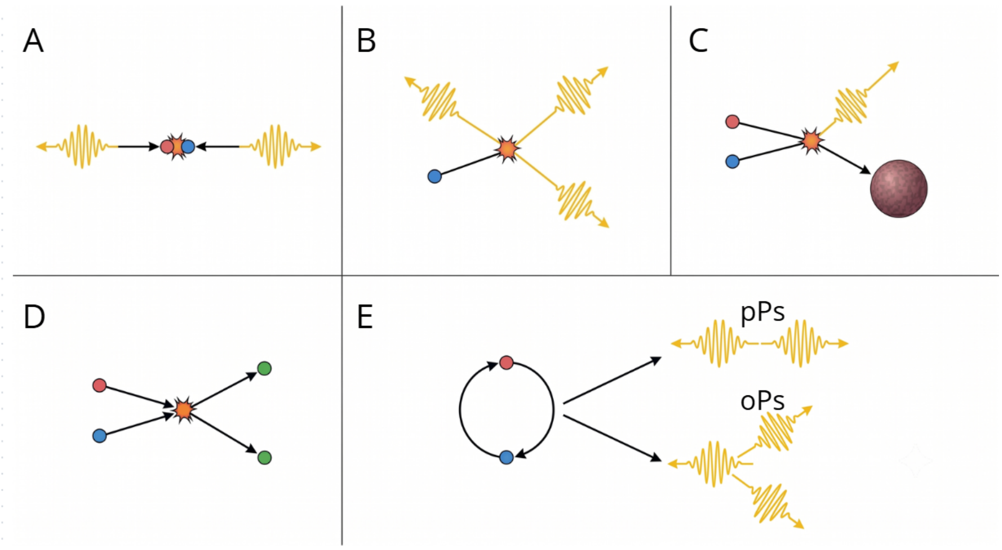

Figure 2.1: Schematic illustrations presenting different interactions of positrons with matter: A - most common 2 γ annihilation, B - three γ-ray annihilation, C - single quantum annihilation, D - radiationless annihilation, E - positronium formation (with two possibilities, either oPs or pPs).

13:8701517221

In conventional PET imaging, the nearly simultaneous arrival of the two 511 keV gamma rays is detected by a stationary ring of dense scintillator crystals surrounding the patient [14]. This mechanism, known as coincidence detection, allows the system to determine the line of response (LOR) along which the annihilation occurred, eliminating the need for physical collimators and drastically reducing background noise. A valid coincidence event is registered only when two opposing detectors record a photon within a narrow coincidence window, typically on the order of a few nanoseconds [8]. Scintillators are materials capable of absorbing high-energy ionizing radiation and converting it, predominantly through photoelectric effect, into lower-energy visible light photons, which are then amplified into electrical signals by photomultiplier tubes. This is shown schematically in Fig. 2.2.

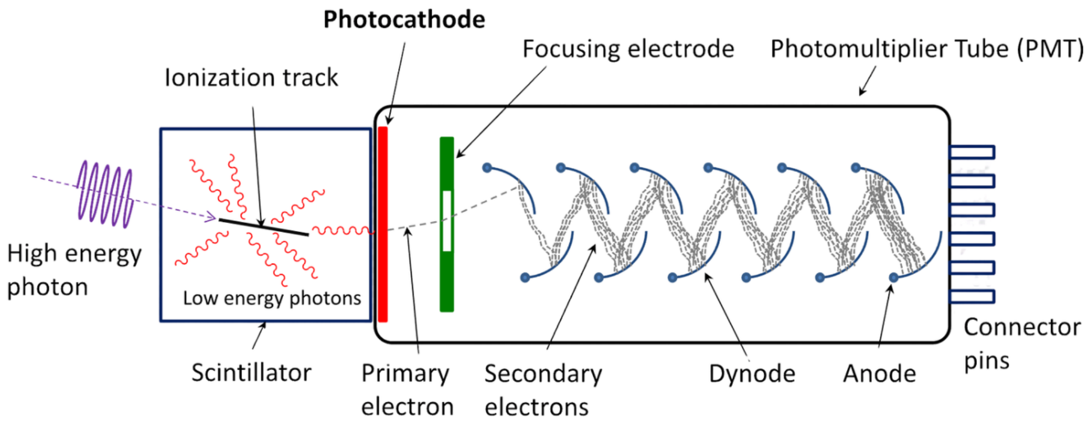

Figure 2.2: Schematic of the scintillation detection principle used in PET detectors. A high-energy photon (511 keV annihilation gamma) interacts with the scintillator crystal, depositing its energy along an ionisation track and producing a flash of low-energy (visible) photons. These photons reach the photocathode of the photomultiplier tube (PMT), where a primary electron is emitted via the photoelectric effect. The electron is then guided by the focusing electrode towards the first dynode, where secondary emission produces an avalanche of electrons at each successive dynode stage. The resulting signal is collected at the anode and read out through the connector pins. Figure adapted from [15].

Modern PET systems employ dense inorganic single-crystal scintillators to achieve high stopping power. The earliest detectors used thallium-doped sodium iodide (NaI[Tl]), but this material was progressively replaced by bismuth germanate (BGO), whose dramatically higher density and atomic number yielded superior detection efficiency for 511 keV gamma rays [16]. Common materials in contemporary systems include BGO, cerium-doped gadolinium oxyorthosilicate (GSO), and cerium-doped lutetium oxyorthosilicate (LSO). The technological shift towards materials like LSO and GSO has been largely driven by their higher light output and significantly shorter decay times compared to BGO — LSO's primary decay constant of 40 ns against BGO's 300 ns — which minimizes dead time and improves spatial resolution [16].

Since there are millions of coincidences during a single PET imaging procedure, errors occur which are related to the proper assignment of the Line of Response (LOR). The first major source of degradation in PET data results from the interactions of γ rays with the tissues within the patient's body. Those interactions happen predominantly via Compton scattering, which alters the photons' energy and direction. Consequently, the photon fails to travel along a straight LOR, being attenuated. However, attenuation correction is possible, and the modern approach includes a CT scan that creates an attenuation map for values at 511 keV, which can be paired with the PET image, yielding accurate results [17].

The second source of error in PET imaging leading to the creation of a false LOR is random coincidences. Those coincidences occur when two photons from separate annihilation events are detected within the same coincidence time window (CTW). These events do not carry spatial information; instead, they contaminate the image with reduced contrast and artifacts [17, 18]. One way to correct such coincidences is the delayed time window technique (DTW). The basic principle of this technique is to delay the signals from one of the detectors so that true coincident events fall outside the resolving time of the circuitry, allowing the measurement of accidental coincidences alone [19].

The third type is scatter coincidences, in which one or both photons have been scattered. In consequence, the resulting LOR does not contain the information about the annihilation point, as such events are incorrectly positioned [17]. Therefore, the produced PET image is further degraded, biased, and suffers from reduced contrast. To overcome this issue, another correction method can be employed, for example, a Monte Carlo-based technique which simulates possible photon interactions and accounts for them in the reconstructed PET image [18]. All the primary coincedences are shown in Fig. 2.3.

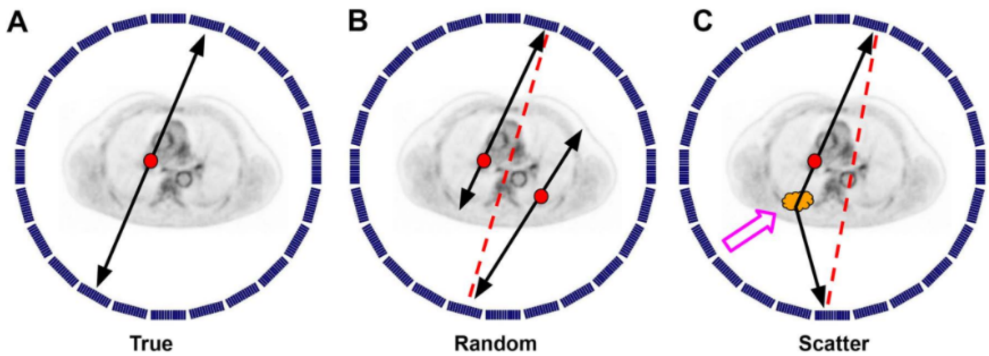

Figure 2.3: Three primary coincedences that occur during the PET imaging procedure detected by the system. Panel A shows true coincedences where both photons originate from the same annihilation event and are detected without scattering; B shows random coincedences, where photons from different annihilation events are detected; C - Scatter coincedences where at least one photon undergoes scattering before detection. Figure adaptet from [18]

2.2 Jagiellonian Positron Emission Tomograph (J-PET)

In the last decade, Positron Emission Tomography has seen significant development with the creation of the Jagiellonian Positron Emission Tomograph (J-PET). It utilizes plastic scintillators instead of relatively expensive crystal-based ones, enabling the construction of cost-effective whole-body scanners. The working principle is analogous to conventional PET: γ rays from an annihilation event interact with the scintillator material, but in J-PET this interaction proceeds only via the Compton effect rather than the photoelectric effect in crystal detectors [20]. Visible light photons travel along the plastic strip to photomultipliers coupled at both ends. The position of interaction is determined from the time difference of the light signals arriving at the photomultipliers. Once the interaction points in the scintillators are identified, a line of response (LOR) can be reconstructed along which the positron annihilation occurred, as shown in figure 2.4.

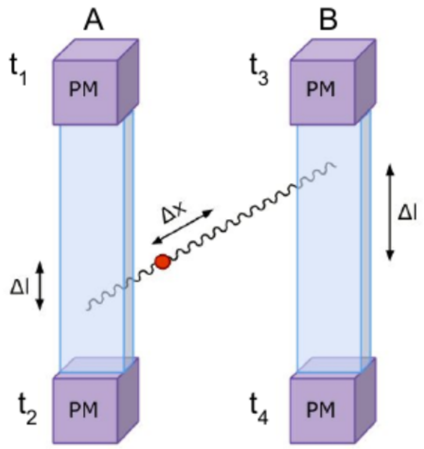

Figure 2.4: Principle of position reconstruction in J-PET. A γ quantum interacting in a plastic scintillator module produces scintillation light that propagates toward photomultipliers at both ends. The interaction position within the module (Δl) is derived from the difference in light arrival times (t_1, t_2). Once interaction points in two modules (A and B) are known, the line of response (LOR) is established, and the annihilation position along it (Δx) is obtained from the time-of-flight difference between the two modules. Thus, both Δl and Δx are determined entirely from timing information. Figure is adapted from [20]

However, cost reduction is not the only advantage of J-PET. The decay constant of plastic scintillator light pulse is 1.8 ns [20]. It enables superior timing resolution and reduces pulse pile-up relative to crystal-based detectors. To achieve rapid energy deposition estimation, the Time Over Threshold (TOT) method was introduced, which probes the signal at four constant thresholds to further improve this estimation. The first prototype achieved a coincidence resolving time (CRT) of 490 ps [20]. Timing resolution is essential for positronium imaging, where the ortho-positronium (o-Ps) lifetime in tissues is only a few nanoseconds (∼2.72 ns for healthy tissue and ∼1.77 ns for glioma tumors) [13].

Time resolution alone does not make J-PET suitable for positronium imaging; another key contribution lies in the trigger-less data acquisition mode. Unlike conventional PET systems that rely on hardware triggers to select only standard two-photon annihilation events, J-PET continuously records all signals from the detector, including those that would otherwise be discarded at the acquisition level. This allows the detection of prompt gamma quanta emitted at the moment of positronium formation, which happens in 40% of cases in the human body. The ability to capture these non-classical events is essential for determining the positronium formation time, a prerequisite for the developing technique of Positronium Lifetime Imaging (PLI) [13, 21, 20].

2.3 Radioisotopes Requirements

The positrons used in the PET imaging procedure are not naturally occurring particles within our bodies. They are the products of β^+ decay, also known as positron emission. In this process, an unstable atomic nucleus with an excess of protons relative to neutrons converts a proton into a neutron. This is driven by the weak interaction, and, as a byproduct, a positron and an electron neutrino are emitted [22]. So, a nuclide with a high branching ratio for β^+ decay is needed for PET imaging.

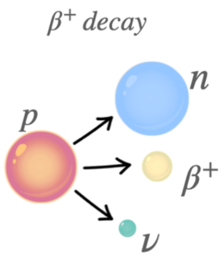

Figure 2.5: Schematic showing the particles involved in β^+ decay. In the nucleus the proton changes to neutron as it is energetically favourable, during the transition a positron (anti-electron) and neutrino are emitted. Figure adapted from [23]

Another important factor that must be taken into consideration during the radioisotope selection is the half-life. It should be long enough to account for the time of its preparation, transport, injection and the imaging procedure, but also short enough to avoid excessive radiation burden to the patient [24].

Very important are also the chemical properties of a radionuclide, which should easily bind to its biological carrier inside the human body. Together they form a radiotracer which should exhibit high affinity for its target; one such example is 2-deoxy-2-[18F]fluoro-D-glucose ([^{18}F]FDG) which is rapidly uptaken in cancerous tissues, allowing good tumor imaging [25].

Despite the dominant position of ^{18}F in clinical PET, which accounts for approximately 86% of all scans performed worldwide, there is a growing interest in radionuclides beyond the conventional short-lived emitters. This trend is driven primarily by the expanding concept of theranostics, in which the same radiopharmaceutical is used for both diagnostic imaging and targeted radionuclide therapy. For such an approach, chemically identical isotopes of a given element are required: one emitting positrons for PET imaging and another emitting beta or alpha particles for therapy. Scandium is a particularly promising candidate in this context, as ^{43}Sc and ^{44}Sc can serve as PET imaging partners to the therapeutic ^{47}Sc, all sharing the same chemical properties and thus enabling the use of identical chelators and labelling procedures [26].

In addition to theranostic applications, non-conventional radionuclides offer advantages that stem from their distinct physical properties. Isotopes with longer half-lives, such as ^{89}Zr ($t_{1/2} = 78.4$ h) and ^{124}I ($t_{1/2} = 100.2$ h), make it possible to label slow-circulating biomolecules such as monoclonal antibodies, which require hours to days for adequate tumour uptake and are unsuitable for imaging with the 110-minute half-life of ^{18}F [27]. Generator-produced isotopes like ^{68}Ga ($t_{1/2} = 67.7$ h), available from a ^{68}Ge/^{68}Ga generator system, provide PET capability at sites without a dedicated cyclotron and have become widely used in neuroendocrine tumour and prostate cancer imaging [27]. At the same time, the use of radionuclides with higher positron energies and more complex decay schemes introduces new challenges. For example, ^{68}Ga and ^{82}Rb emit positrons with maximum energies of 1.90 and 3.36 MeV respectively, substantially exceeding the 0.63 MeV of ^{18}F. These higher energies result in a larger positron range, which degrades spatial resolution, and are often accompanied by prompt gamma emissions that can create additional coincidences and compromise quantitative accuracy [27].

Yet, both conventional and non-conventional radiotracers should clear readily from the body and, together with their daughter nuclides, be as non-toxic as possible. Some common radionuclides with their characteristics are presented in the Tab. 2.1.

One of the emerging radioisotopes is ^{44}Sc, a promising candidate for positronium lifetime imaging (PLI) [26, 29]. It has a clinically compatible half-life of 4.04 h and a high branching ratio for positron emission of 94.3%. Most critically for PLI, however, upon positron emission it also emits a 1157 keV prompt γ-ray with an approximate yield of 100%. The prompt gamma thus serves as a timing marker for positronium formation, while the two 511 keV annihilation photons signal the time of its decay - together enabling the positronium lifetime to be determined on an event-by-event basis [30]. Moreover, ^{44}Sc with its maximum energy standing at 1.47 MeV fits in the middle of positron energies for already used radioisotopes - with the convential radioisotope of ^{82}Rb having $E_{\beta+,\max}$ equal to 3.36 MeV, being used in 6% of cases, and most popular ^{18}F, which has the lowest maximum energy of 0.63 MeV, used in 86% od PET imaging procedures.

Table 2.1: Properties and clinical applications of commonly used PET radionuclides, with estimated frequency of use based on 2023 clinical data [28, 25].

Radionuclide	Half-life	Decay mode (β^+)	$E_{\beta^+,\max}$ (MeV)	Share (%)	Primary clinical application
^{18}F	109.8 min	97% β^+, 3% EC	0.63	86%	Oncology - [^{18}F]FDG for glucose metabolism; Pylarify, NaF
^{11}C	20.4 min	100% β^+	0.96	<1%	Neurology - receptor imaging (e.g. raclopride)
^{13}N	10.0 min	100% β^+	1.20	<1%	Cardiology - [^{13}N]ammonia for perfusion
^{15}O	2.0 min	100% β^+	1.73	<1%	Perfusion - [^{15}O]water, gold standard for CBF
^{68}Ga	67.7 min	89% β^+, 11% EC	1.90	6%	Oncology - PSMA-11 (prostate), DOTATATE (NET)
^{82}Rb	1.3 min	95% β^+, 5% EC	3.36	6%	Cardiology - myocardial perfusion
^{64}Cu	12.7 h	17% β^+, 44% EC	0.65	2%	Oncology - immuno-PET, hypoxia imaging
^{44}Sc	4.0 h	94% β^+, 6% EC	1.47	<1%	Emerging PLI - positronium lifetime imaging
^{89}Zr	78.4 h	23% β^+, 77% EC	0.90	<1%	Immuno-PET - antibody labeling
^{124}I	100.2 h	23% β^+, 77% EC	2.13	<1%	Thyroid cancer, immuno-PET

2.4 Positron Range

As mentioned in section History and principles of PET, the physical resolution limit for PET imaging is the positron range. What is even more significant is that the correction of spatial blurring arising from positron range is not yet well established. As seen in Table 4 in [31], very different values are reported, even within the scope of Monte Carlo simulations which are all based on the same physical principles. Moreover, comparing simulation results with ranges obtained from experiments, a different problem emerges: simulations cannot determine positron ranges that match experimental data. Therefore, of all the effects that contribute to image quality, the most uncertain and poorly understood is the positron range. This effect can be the most prominent contributor to spatial resolution degradation for certain isotopes and detectors [4].

The positron range is the distance a positron travels from its point of emission to its point of annihilation. After being emitted from the nucleus, the positron loses kinetic energy through inelastic collisions with atomic electrons (ionisation) and elastic scattering on atomic nuclei (multiple Coulomb scattering). Once it has thermalised, it annihilates with an electron. The distance travelled depends primarily on two factors: the initial kinetic energy of the positron and the density and atomic composition of the surrounding medium. The initial energy is not a single value but a continuous spectrum ranging from zero up to a maximum energy E_{max}, characteristic of the decaying isotope. The shape of this spectrum is described by the Fermi theory of beta decay, and for allowed transitions the number of decays at a given energy E is given by:

$$N(E)\,dE = g \cdot F(Z, E) \cdot p \cdot (E + 1) \cdot (E_{\mathrm{max}} - E)^2\,dE, \tag{2.1}$$

where $F(Z, E)$ is the Fermi function accounting for the Coulomb field of the daughter nucleus, p is the positron momentum, and g is a coupling constant [31]. The spectrum is peaked toward lower energies, meaning that a significant fraction of emitted positrons have considerably less energy than E_{max} [4]. As a result, the mean positron energy E_{mean} is typically about one third of E_{max}, and the shape of the spectrum varies between isotopes. Consequently, as pointed out by Jødal et al. [6], the endpoint energy E_{max} alone is insufficient to characterise the potential image quality of a given PET isotope - the full energy spectrum must be taken into account.

To illustrate the differences between a low-energy and a higher-energy positron emitter, Table 2.2 compares physical properties of ^{18}F and ^{44}Sc, which were the scope of research described in this thesis. The shorter positron range of ^{18}F (mean range of approximately 0.6 mm in water) makes it the gold standard for high-resolution imaging. In contrast, ^{44}Sc, with a mean positron energy of 632 keV, has a mean range of approximately 2.3 mm in water [32, 33]. This is a result of its higher endpoint energy of 1474 keV. Although still lower than that of ^{68}Ga (mean range of approximately 2.9 mm), the positron range of ^{44}Sc is nearly four times larger than that of ^{18}F, which means that the spatial blurring introduced by positron range is substantially more pronounced for ^{44}Sc and must be carefully accounted for.

Table 2.2: Comparison of positron emission properties of ^{18}F and ^{44}Sc. Data for ^{18}F from [31, 4]; data for ^{44}Sc from [32, 33].

Property	^{18}F	^{44}Sc
Half-life	109.8 min	3.97 h
E_{max} (keV)	634	1474
E_{mean} (keV)	250	632
Mean positron range in water (mm)	0.6	2.3
β^+ branching ratio (%)	96.7	94.3

The disagreement between simulated and experimentally measured positron ranges further complicates the picture. Champion and Le Loirec [31] reported that their Monte Carlo results for mean positron range differed from the experimental data of Cho et al. [34] by 13.5% for ^{11}C and by over 60% for ^{82}Rb. These discrepancies likely arise from differences in the description of positron transport between Monte Carlo simulations, the accuracy of the underlying interaction cross sections, and the description of the medium. For non-conventional isotopes such as ^{44}Sc, experimental range measurements are scarce, and the available data come almost exclusively from simulations, which adds uncertainty to the correction of range-induced blurring in image reconstruction.

One aspect on which the literature does agree is that the negative impact on spatial resolution is more pronounced for radioisotopes with higher positron energies [4, 31, 35]. In recent years, resolution-recovery algorithms have become available that account for resolution-degrading effects through isotope-specific point spread functions [6]. However, as Jødal et al. [6] point out, a point spread function measured for one isotope (e.g. ^{18}F) will not correctly represent the blurring from an isotope with a significantly different mean energy. Therefore, extensive research is needed especially for higher-energy positron emitters, so that during post-processing the positron range can be accounted for in image reconstruction and thereby improve spatial resolution [36, 6].

3 Materials and Methods

3.1 Experimental Setup

The experiment was conducted using the modular J-PET scanner [30]. The tomograph consists of 24 independent detection modules arranged in a circle with a diameter of 73.9 cm. Each module is composed of 13 plastic scintillator strips (BC-404) with dimensions of $24 \times 6 \times 500$ mm^3, providing an axial field-of-view (AFOV) of 50 cm [37]. To maximise light transmission and prevent light leakage, the strips are wrapped in Vikuiti Enhanced Specular Reflector (ESR) foil and DuPont Kapton 100B film. Each scintillator strip is read out on both ends by four Hamamatsu-S13 Silicon Photomultipliers (SiPMs) with an active area of 6×6 mm^2 each. When a γ quantum interacts in a scintillator, four timestamps are generated per SiPM - two at the leading edge and two at the trailing edge of the signal. The timestamps are continuously recorded by a trigger-less Data Acquisition System (DAQ) capable of handling data streams of up to 8 Gbps, which is designed to register multiphoton events [13, 37]. The use of plastic scintillators provides superior timing properties (0.5 ns rise time and 1.8 ns decay time) compared to crystal-based detectors, while the Time-over-Threshold (TOT) method is utilized as a faster energy estimation technique enabling continuous data collection without dead time [20].

The event selection criteria, described in detail in [29, 13], allow a clear separation between events from ortho-positronium (o-Ps) decays and standard two-photon annihilations. In this study, only two-photon annihilation events were used for further analysis. For both ^{18}F and ^{44}Sc, the selection began with a TOT cut corresponding to an energy deposition range of approximately 200-370 keV, which rejects events from scattered γ quanta while retaining the majority of valid annihilation photons [38]. In the case of ^{44}Sc, an additional energy threshold above 370 keV was applied to identify prompt γ rays (1157 keV) for positronium lifetime imaging; however, for the two-photon imaging discussed in this work, only events within the standard annihilation window were used. So, the TOT signal range from 5.5 to 8 ns $\circ$ V was applied to determine events, subsequently used in this work [30].

A coincidence time window (CTW) of 20 ns was chosen for event pairing, which is consistent with the timing resolution of the modular J-PET system. Furthermore, the requirement for position of two interactions from the same coincedence to have an angular separation greater than 60 degrees in the trans-axial direction was applied [18]. The trigger-less acquisition mode allowed all registered hits to be stored and processed offline, with the J-PET Framework software handling time calibration, hit reconstruction, and event building. After event selection and coincidence processing, the data aquired were converted

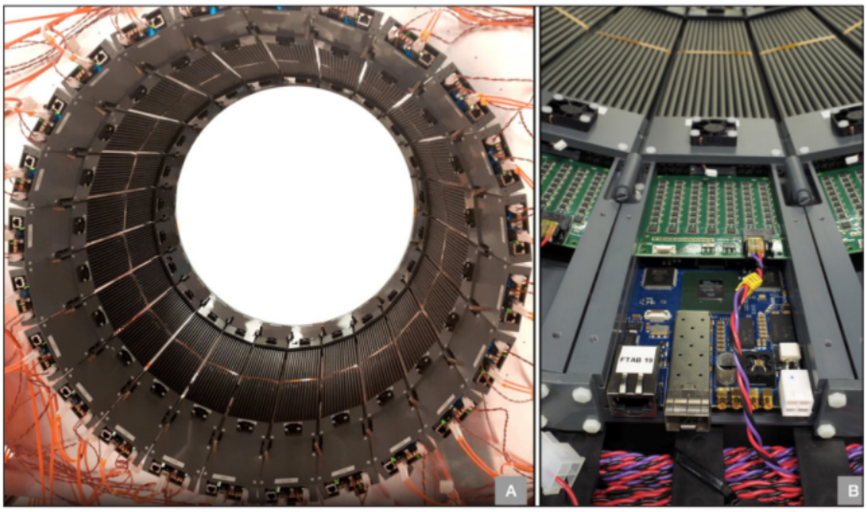

Figure 3.1: The Modular J-PET tomograph. Panel (A): front view of the detector gantry, showing the cylindrical arrangement of plastic scintillator modules with silicon photomultiplier (SiPM) readout, forming the imaging space into which the phantom or patient is inserted. Panel (B): front-end electronics, including the frontend signal processing boards and the data acquisition system responsible for coincidence detection and time stamping of annihilation events.

into a list-mode file for CASToR, an open source reconstruction software. For the image reconstruction the Maximum Likelihood Expectation Maximization (MLEM) algorithm was used, which has ran for 10 iterations. The data were saved as NIfTI files with a voxel size of $2.5 \times 2.5 \times 2.5$ mm^3, a matrix of $200 \times 200 \times 200$ voxels and uniform gaussian filter of 5 mm for further analysis [18, 30].

For the two-isotope imaging, a National Electrical Manufacturers Association Image Quality (NEMA IQ) phantom was used (Fig. 3.3). The phantom consists of six spheres with inner diameters of 10, 13, 17, 22, 28 and 37 mm and a plastic boundary with a thickness of 1 mm, as well as a lung-equivalent insert filled with styrofoam balls. During the experiment, the background compartment was filled with distilled water.

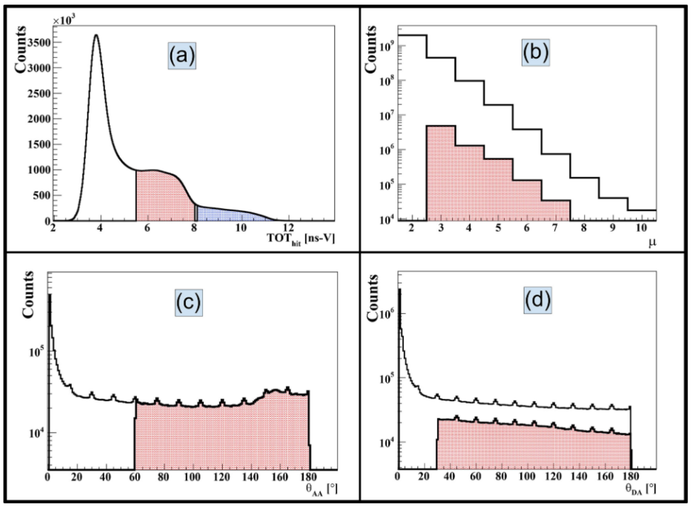

Figure 3.2: Event selection criteria used to isolate two-photon annihilation events. Panel (a) shows the time-over-threshold (TOT) distribution for all registered hits; the shaded (red) region marks the accepted energy window of 200-370 keV, which retains the majority of valid annihilation photons while suppressing scattered γ quanta. Panels (b), (c), and (d) present the distributions of the multiplicity parameter μ, the angular separation between two annihilation photons θ_{AA}, and the angular separation between each annihilation photon and the de-excitation γ quantum θ_{DA} (which was not utilized in this work), respectively; the red-highlighted subsets correspond to events that pass all selection cuts and constitute the final two-photon annihilation sample used for image reconstruction. Figure adapted from [30].

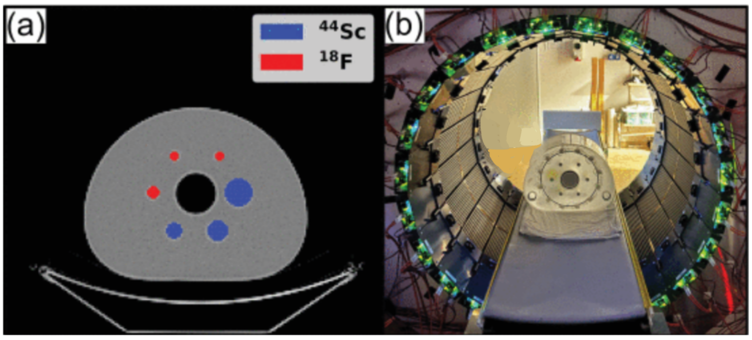

Figure 3.3: (a) Transaxial CT scan of the NEMA IQ phantom, giving overview of radiotracer distribution in spheres. The red cicrles are denoting fluorium-filled spheres, while the blue ones denote the scandium-filled spheres.(b) NEMA IQ phantom positioned inside the modular J-PET scanner. Figure adapted from [30].

The three smaller spheres - 10, 13 and 17 mm - were filled with a water solution of ^{18}F at an activity concentration of 0.574 MBq/mL at the start of the experiment for each sphere [30].

The three larger spheres were filled with a water solution of ^{44}Sc at an activity concentration of 0.185 MBq/mL. The radioisotope was produced by the Heavy Ion Laboratory of the University of Warsaw via the ^{44}Ca(p,n)^{44}Sc reaction [30].

Prepared phantom was then positioned inside the tomograph, as shown in Fig. 3.3. The data were acquired for 178 min and processed offline. For subsequent analysis in this work, the NIfTI files obtained from the measurement were used.

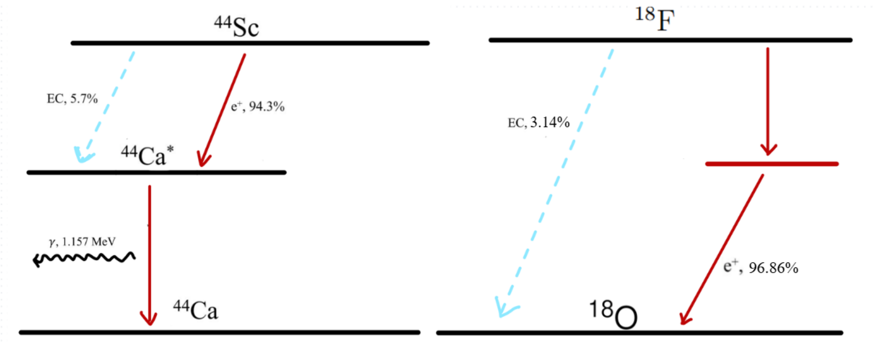

Figure 3.4: Decay schemes of ^{44}Sc and ^{18}F. ^{44}Sc (half-life 3.97 h) decays via β^+ emission (94.3%) and electron capture (5.7%) to stable ^{44}Ca, with a mean positron energy of 632 keV and a maximum positron energy of 1474 keV. The de-excitation of the daughter nucleus is accompanied by a prompt γ ray at 1157 keV emitted in 100% of decays, which enables positronium lifetime imaging. ^{18}F (half-life 109.7 min) decays via β^+ emission (96.86%) and electron capture (3.14%) directly to the ground state of stable ^{18}O, with a mean positron energy of approximately 250 keV and a maximum of 633 keV; no prompt γ rays are emitted in its decay.

3.2 Monte Carlo Simulations

Monte Carlo simulations were prepared to see whether for ^{44}Sc the effect of simulation underestimating the spatial resolution is present. As a reference, the simulations were also carried out for ^{18}F to ensure proper methodology. All the programs used to develop the simulation are available on github [39]. The positron ranges were calculated using two different approaches - the maximum range based on [40], given by:

$$X = \frac{0.412 \cdot E^{(1.265-0.0954 \cdot \ln E)}}{\rho}. \tag{3.1}$$

This equation is a semi-empirical range-energy relation that does not account for multiple scattering within the material and treats the distance between emission and annihilation as a straight line. The second approach was the calculation of the mean positron range, which takes into account changes in the positron direction due to scattering, resulting in a shorter net distance between emission and annihilation than the actual path travelled by the positron [36]. The formula averages these effects and is given by:

$$R_{\text{mean}} = \frac{0.108 \cdot E^{1.14}}{\rho}. \tag{3.2}$$

In both equations E is the positron energy (in MeV) and ρ is the material density.

The simulations started with the generation of energy spectra from which positron energies were sampled for use in the range equations. The spectra were produced using equation 2.1, with the allowed Fermi function for lighter elements taken from [41] and equal to:

$$F_{\text{allowed}}(Z,E) = \frac{2\pi\eta}{1-e^{-2\pi\eta}}, \quad \text{with} \quad \eta = -Z\alpha E/p. \tag{3.3}$$

In the equation η is . The spectra, normalized to unity, are shown in Fig. 3.5.

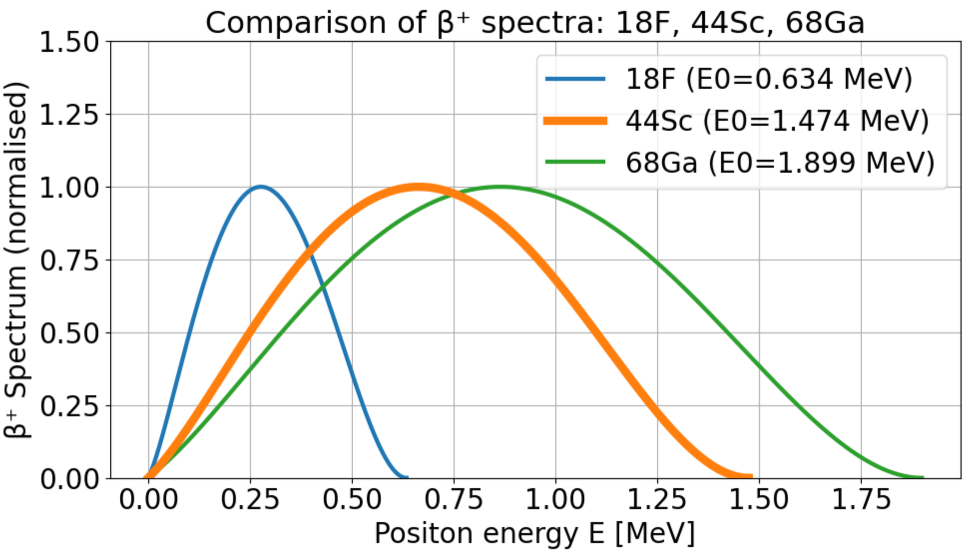

Figure 3.5: Energy spectra of ^{18}F, ^{44}Sc and ^{68}Ga (for reference) calculated in Python. The spectra were all normalized to unity to improve readability. The endpoint energies used to produce the spectrum were taken from [4, 42, 43].

Next, the positron emission points were simulated using the random function from the NumPy random library. For each isotope, every sphere of the NEMA IQ phantom was defined so that emission starting points were uniformly sampled within the inner radius of each sphere. To ensure the proper distribution, emission points were simulated in spherical coordinates and then recalculated to Cartesian ones. Example histograms (for ^{18}F in the 10 mm sphere) are provided in Fig. 3.6 to confirm the correct emission point distribution. To make the data comparable with the experimental setup, a different number of points was simulated for each sphere to ensure the same activity concentration within all spheres. Thus, for the smallest sphere, 1 million positions were generated for both isotopes, while for the largest sphere the number grew to 50.6 million events.

Since inside the spheres positrons are not "aware" of which direction points toward the centre and which toward the boundary, the direction vectors for each emission point had to be uniformly simulated as well. Again, the random function was used to generated with the random function and their lengths equaled to one. The direction vectors were randomised

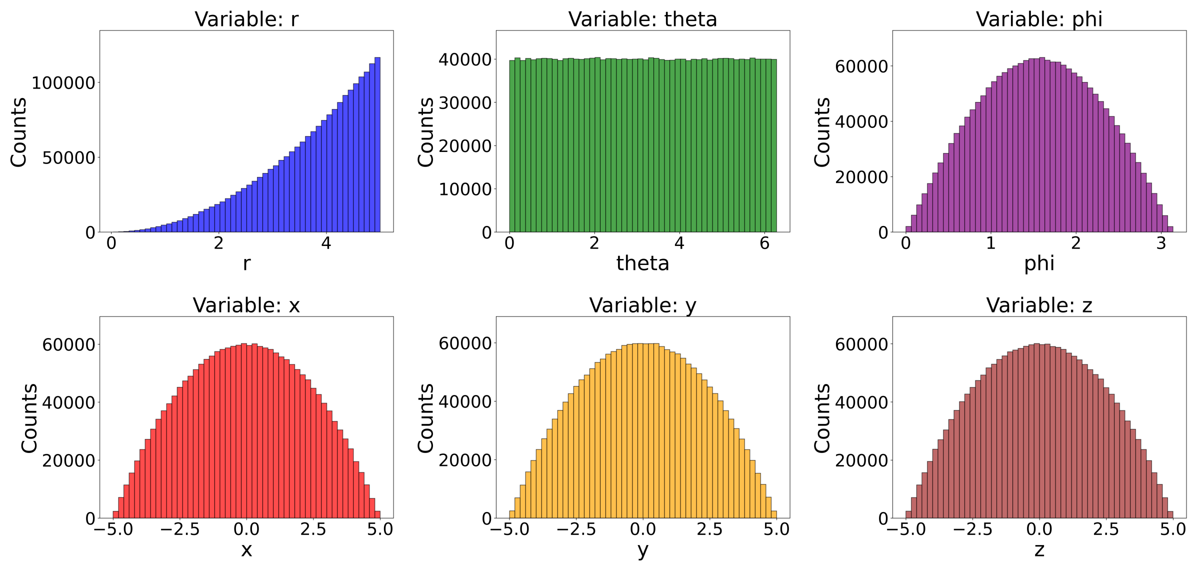

Figure 3.6: Verification of uniform emission point generation within the NEMA IQ phantom spheres, shown here for the 10 mm sphere with ^{18}F. Top row: distributions in spherical coordinates. The radial coordinate r follows an r^2-weighted distribution consistent with uniform volumetric sampling, the azimuthal angle θ is uniformly distributed over $[0, 2\pi)$, and the polar angle ϕ follows a $\sin\phi$ distribution, as expected for isotropic emission from a sphere. Bottom row: projections onto Cartesian axes x, y, and z, each exhibiting the characteristic dome-shaped profile of a uniform sphere. The flat (green) and symmetric (red, orange, brown) histograms confirm that no directional bias was introduced during the starting point generation.

based on spherical coordinates and later converted to Cartesian coordinates. This generation step is visualized with histograms in Fig. 3.7.

The last preparation step before the actual simulation was the calculation of the initial range. In one version of the simulation protocol, it was calculated using equation 3.1 and in the other using equation 3.2. In both cases, the energies needed to calculate the ranges were sampled from the produced spectra (Fig. 3.5). To confirm proper energy sampling, histograms for both ^{18}F and ^{44}Sc were produced (shown in Fig. 3.8) for an example sphere of inner diameter 10 mm. As can be seen, the energies in the simulation recreate the theoretical spectra, confirming that the randomisation was successful and physically applicable.

To determine the annihilation points, ray-tracing was performed. Taking the simulated starting point, direction vector and range, the code "followed" each positron to determine its stopping (annihilation) point in 3D, depending on which range equation was implemented. If any positron reached the inner wall of a NEMA IQ phantom sphere, a mask was applied due to the higher density of the plastic wall (ρ = 1.18 g/cm^3), which influences the positron range. Thus, positrons were divided into three groups - those that stayed inside the sphere, those that stopped in the plastic wall, and those that escaped into the surrounding environment. Bar charts presenting the intermediate results, along with their visualisations, can be found in Appendix 1.

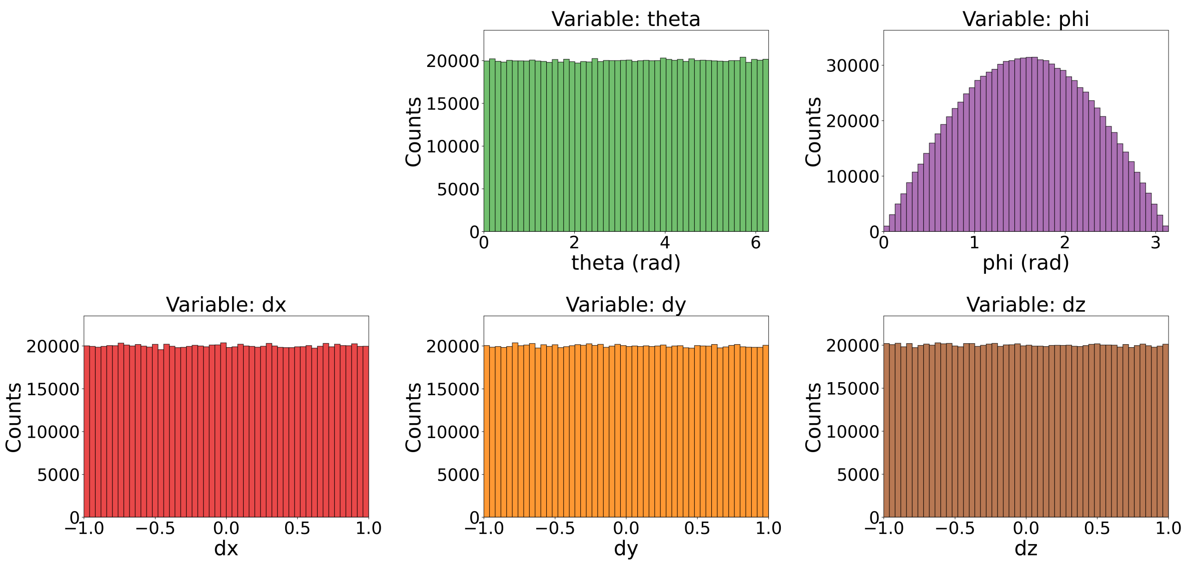

Figure 3.7: Verification of isotropic direction vector generation for positron propagation, shown here for the 10 mm sphere with ^{18}F. Top row: angular distributions of the generated direction vectors. The azimuthal angle θ is uniformly distributed over $[0, 2\pi)$ and the polar angle ϕ follows a $\sin\phi$ distribution, both consistent with isotropic emission on the unit sphere. Bottom row: Cartesian components d_x, d_y, and d_z of the unit direction vector, each exhibiting a uniform distribution over $[-1, 1]$. This is the expected projection of isotropic directions onto any single axis and confirms the absence of directional bias in the generated vectors.

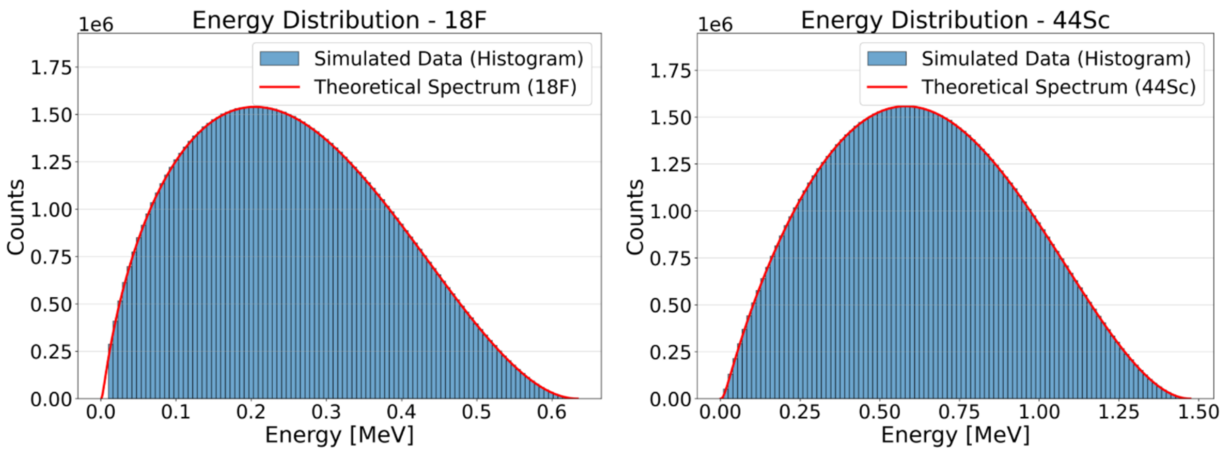

Figure 3.8: Energy histograms for ^{18}F (left) and ^{44}Sc (right). Over the histogram a theoretical spectrum is drawn using the equation 2.1. The alignement of histogram bars (blue) with theoretical spectrum line (red) confirms the absence of energetical bias in the sampled energies during the simulation procedure.

Finally, the simulated data were saved as NIfTI files with the same parameters as the data received from the experiment: the positron annihilation points were voxelised into a $200 \times 200 \times 200$ matrix, with each voxel being a cube of size $2.5 \times 2.5 \times 2.5$ mm. Additionally, a 3D Gaussian filter was applied to match the effective spatial resolution of the

PET system [18]. The filter width was set to a full width at half maximum (FWHM) of 2 voxels, corresponding to $\sigma = \mathrm{FWHM}/(2\sqrt{2\ln 2}) \approx 0.85$ voxels, and implemented using the *scipy.ndimage.gaussian_filter* function. From the prepared NIfTI files, a plane along the z-axis with the maximum voxel intensity was identified. This plane was saved as a maximum intensity slice in PNG format and subsequently analysed to determine the diameters of the spheres in the reconstructed images.

3.3 Sphere Diameter Determination

The five files (one from experiment, and one for each isotope in two different range calculation modes - Appendix 2) were analysed in order to determine the sphere diameters. Initially two approaches were considered.

The first approach employed an algorithm that determined the diameters directly from the NIfTI files. The script identified bright areas by detecting voxels with intensity greater than 5% of the total intensity, and grouped neighbouring elements into distinct objects - the six NEMA IQ phantom spheres. Then, to eliminate the effects of background, the code found the brightest voxel in each object and discarded voxels with brightness below half of this local maximum. The remaining voxels were recalculated to physical volume in mm^3. From the volume, the radius and subsequently the diameter were reconstructed. The error was defined as twice the standard deviation of the distance between the centre of the sphere and its boundary. However, this method provided unsatisfactory results: for the two largest spheres the regions merged into a single shape (Fig. 3.9), so the obtained diameters were incorrect.

The second method determined the diameters from the PNG files. The script first identified the six brightest regions and defined them as regions of interest (ROIs). Each ROI was cut out from the original PNG file into separate auxiliary PNG files - one for each sphere. After a sphere was isolated, its pixel intensities were set to zero so that it would not be considered when finding the next ROI. Next, for each sphere, pixels with intensity above 20% of the 99th percentile intensity value were used to create a mask for finding the sphere centre. The centre was determined as a weighted sum over pixel positions in the XY plane, with the pixel intensities as weights. This approach ensured that even with smoothed data [44], the centre of gravity would provide the exact centre. Finally, intensity profiles were drawn in steps of 5°, and points where the signal fell below x% of the maximum intensity were treated as the sphere boundaries.

The final diameter was calculated as an arythmetical average of the intensity profiles. Since the intensity could drop between pixels, interpolation was added so that the sphere edge could be located between pixels. The interpolation was performed with a step size of $dr = 0.2$ pixel. The resulting error had two components: the statistical error of the measured diameters (standard deviation) and the systematic error arising from the finite

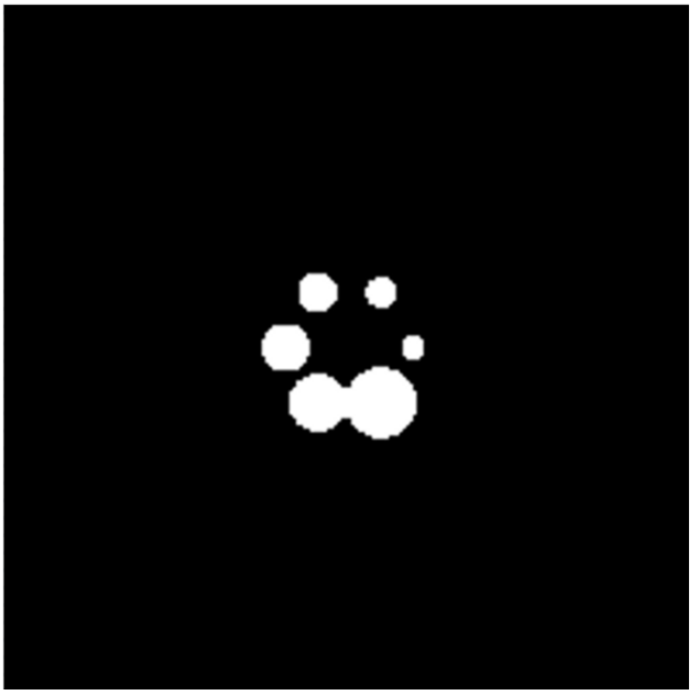

Figure 3.9: Merged 37 and 28 mm spheres from the NEMA IQ Phantom for the diameter determination approach where the ROIs were identified directly in the NIfTI file. The image provides the reason why this method of diameter determination was discarded and the other approach was used.

sampling density. In the program, it was assumed that the error in the edge position follows a uniform distribution over an interval of width dr, yielding the standard deviation:

$$\sigma_{\text{interpolation}} = \frac{dr}{\sqrt{12}}. \tag{3.4}$$

This expression corresponds to the standard uncertainty for a rectangular distribution, as recommended by the Guide to the Expression of Uncertainty in Measurement (GUM) for cases where only the bounds of the interval are known [45].

Since it was suggested in [6] that for simulations the 50% intensity metric can underperform during image reconstrution, in this work the diameters were determined for pixels intesities from 10% to 90% (in steps of 10%) of the maximal intensity, to quantify this effect.

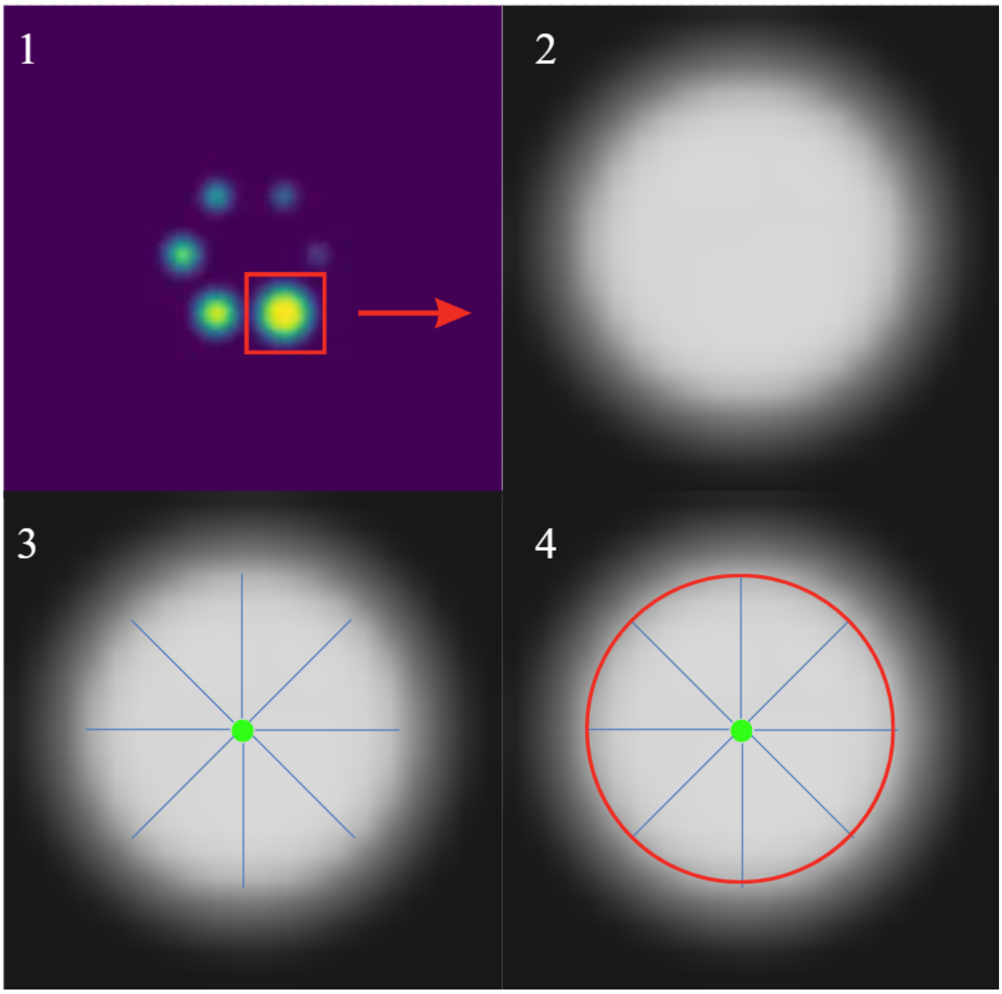

Figure 3.10: A diagram schematically depicting the workflow behind the diameter determination. 1 - from the maximum intensity slice from the NIfTI file a sphere is isolated; 2 - the center of gravity of the sphere is determined; 3 - the intensity profiles drawn from the center untill reaching a point of threshold; 4 - circle with the estimated diameter.

4 Results

4.1 Experimental Data

Since the first threshold that gave non-zero results for all spheres was 40%, this threshold is regarded as the minimal threshold for which data are interpretable. It also indicated that the background pixel intensity was between 30% and 40% of the defined local maximum. Similarly, the last interpretable threshold was 80%, as the 90% threshold returned a value of 0 for the largest spheres in each measurement modality. This occurs because larger spheres have a plateau of intensity, rather than a peak and steep "hills" in the intensity profile, as seen in the smaller spheres. The statistical noise of intensity on this plateau causes the geometric center - the point of origin of the radial search vectors - to fall below 90% of the maximum intensity. Consequently, the algorithm evaluates the initial starting point as already residing outside the sphere's boundary, resulting in an immediate failure to detect the edge.

Figure 4.1 illustrates the reconstructed diameters from experimental data, which consisted of NEMA IQ Phantom spheres filled with either ^{18}F (three smallest spheres - 10, 13 and 17 mm) or ^{44}Sc (thre bigger spheres - 22, 28 and 37 mm). Together with Table 4.1, where exact diameters from reconstructed images are given with uncertainties, they give the complete results from the experimental part of this work.

As can be seen on 4.1, a clear trend emerged. The reconstructed diameters for the three smallest spheres - which were filled with ^{18}F - are consistent across all given thresholds, and all values fall within the real diameters when the measurement uncertainty is taken into account. However, for the three larger spheres, the spread is substantially larger, with a clear tendency to overestimate the real diameters. To better illustrate the spread a graph has been made, where on x-axis is the treshold and on y-axis the reconstructed sphere diameter for spheres 17 mm and 22 mm - so the biggest one filled with fluorine and the smallest one for scandium. The graph is presented below (Fig. 4.2).

Steeper slope for the 22 mm sphere filled with ^{44}Sc indicates that for a higher-energy radioisotope, which emits more energetic positrons, the reconstructed image tends to overestimate the actual object size, when standard 50% threshold is chosen. For fluorione the reconstruction algorithm predicted that taking smaller threshold is desirable for proper image reconstruction. Table 4.1 lists the exact values of the reconstructed diameters.

The most accurate results for spheres filled with ^{18}F were obtained with the 50% metric, with the exception of the 17 mm sphere, where the 40% metric gave the best result. These results are consistent with what has been reported in the literature - ^{18}F, owing to its

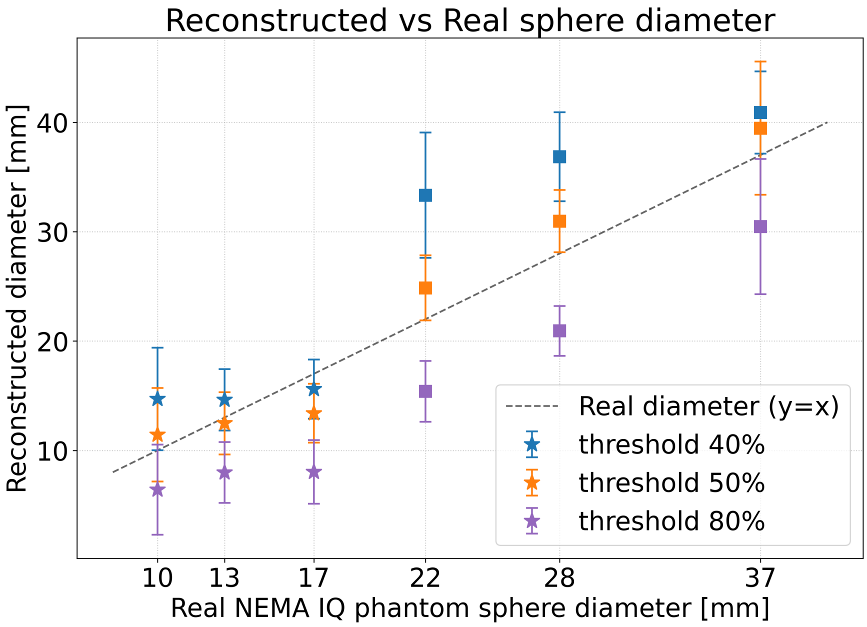

Figure 4.1: Reconstructed diameters from experimental data at selected intensity thresholds (40% -blue, 50% - yellow, and 80% - purple). Only the first, middle, and last interpretable thresholds are shown for readability; a plot with all thresholds is provided in Appendix 3. The star symbol designates the fluorium-filled spheres, while the squares designate the scandium-filled spheres.

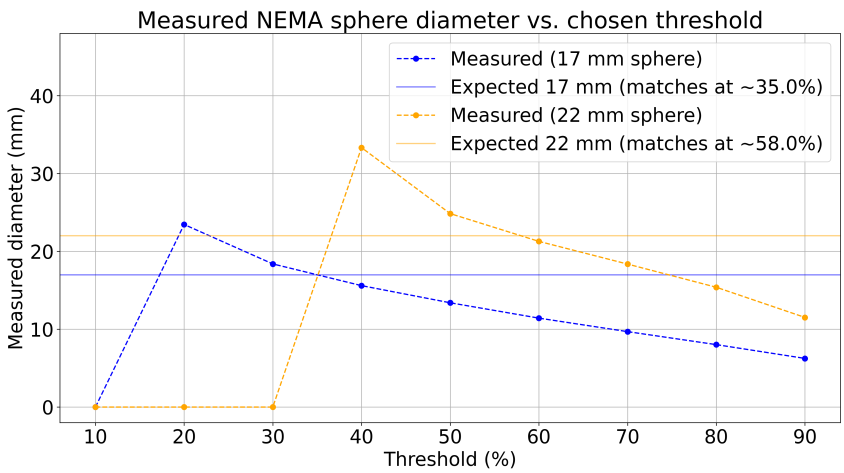

Figure 4.2: Experimental dependence of reconstructed sphere diameter on the intensity threshold for the 17 mm and 22 mm NEMA IQ phantom spheres filled with ^{18}F and ^{44}Sc, respectively. The dashed lines with markers show the measured diameter as a function of threshold, while the solid horizontal lines indicate the true sphere diameters. The 17 mm sphere crosses the expected value at approximately 35%, whereas the 22 mm sphere matches at approximately 58%. At the 40% threshold the 22 mm sphere is significantly overestimated (33.3 ± 5.7 mm), which is a direct consequence of the positron range spill-out from ^{44}Sc. The steep drop of the measured diameter with increasing threshold reflects the Gaussian-like intensity profile of the reconstructed spheres, where stricter thresholds progressively exclude voxels at the sphere boundary.

Table 4.1: Reconstructed diameters and uncertainties for the ^{18}F-filled (10, 13 and 17 mm) and ^{44}Sc-filled (22, 28 and 37 mm) spheres at the 40%, 50% and 80% intensity thresholds.

Real diameter	40%	50%	80%
	d ± s(d) (mm)	d ± s(d) (mm)	d ± s(d) (mm)
37	40.9 ± 3.8	39.5 ± 6.1	30.5 ± 6.2
28	36.9 ± 4.1	31.0 ± 2.9	20.9 ± 2.3
22	33.3 ± 5.7	24.9 ± 3.0	15.4 ± 2.8
17	15.6 ± 2.7	13.4 ± 2.7	8.0 ± 2.9
13	14.7 ± 4.7	12.5 ± 2.8	8.0 ± 2.8
10	14.6 ± 2.8	11.4 ± 4.3	6.4 ± 4.1

low positron energy, produces precise images in terms of object size [4].

The ^{44}Sc-filled spheres, however, show a notable pattern: at the 40% threshold all diameters are significantly overestimated (e.g. 37 mm sphere reconstructed as 40.9 mm, 22 mm sphere as 33.3 mm), while at the 80% threshold the diameters are systematically underestimated (e.g. 37 mm sphere at 30.5 mm). The 50% threshold yields intermediate values closer to the true diameters (e.g. 28 mm sphere at 31.0 mm, 22 mm sphere at 24.9 mm). This progression reflects the broadening effect of the positron range on the reconstructed image: at low thresholds, the inclusion of peripheral background pixels inflates the measured diameter, while at high thresholds the statistical plateau noise causes the algorithm to fail before reaching the true edge. The 60% threshold, which uses a narrower selection of the brightest voxels, provides the most accurate compensation for this effect.

Table 4.2: Best results for the ^{44}Sc-filled spheres, obtained with the 60% intensity threshold.

Real diameter (mm)	d ± s(d) (mm)
37	36.5 ± 6.3
28	27.4 ± 2.5
22	21.3 ± 2.7

4.2 Simulation Data

4.2.1 Maximum Range Mode

To improve readability and comparability with the experimental results, the same three thresholds - 40%, 50% and 80% - were chosen for plotting. Plots with all thresholds are given in Appendix Appendix 4. The results for the maximum range model (described in detail in Section Monte Carlo Simulation) are presented in Figures 4.3 and 4.4.

As can be seen, for both radioisotopes the 50% threshold gives the best results. Moreover, the reconstructed diameters for the remaining two thresholds - 40% and 80% - fall within the uncertainty margins of the real NEMA IQ phantom sphere diameters. The

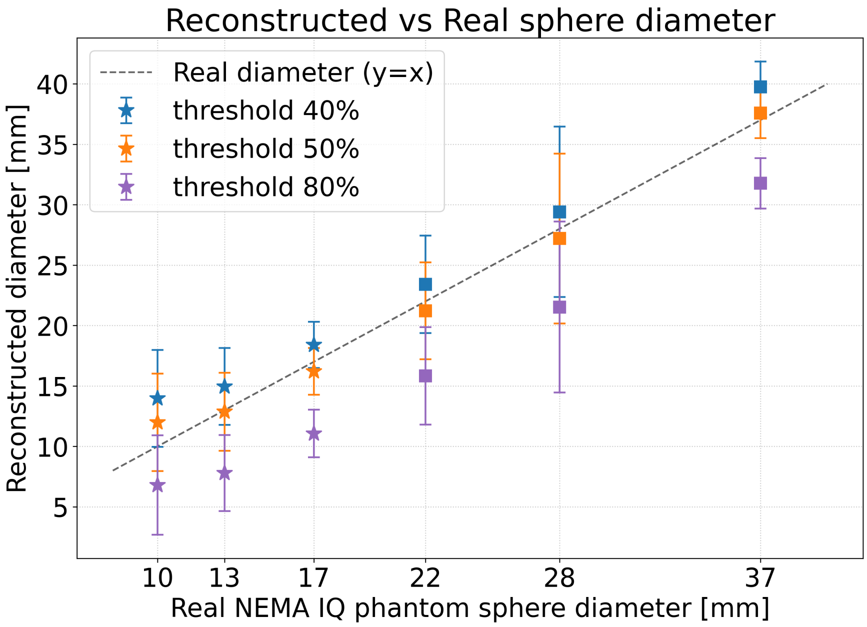

Figure 4.3: Reconstructed diameters from simulated data for ^{18}F with the maximum range mode at selected intensity thresholds (40%, 50%, and 80%). Only the first, middle, and last interpretable thresholds are shown for readability; a plot with all thresholds is provided in Appendix Appendix 4. The treshold 100% would mean that only the pixels with 100% of the maximum intensity are taken into account for the diameter reconstruction.

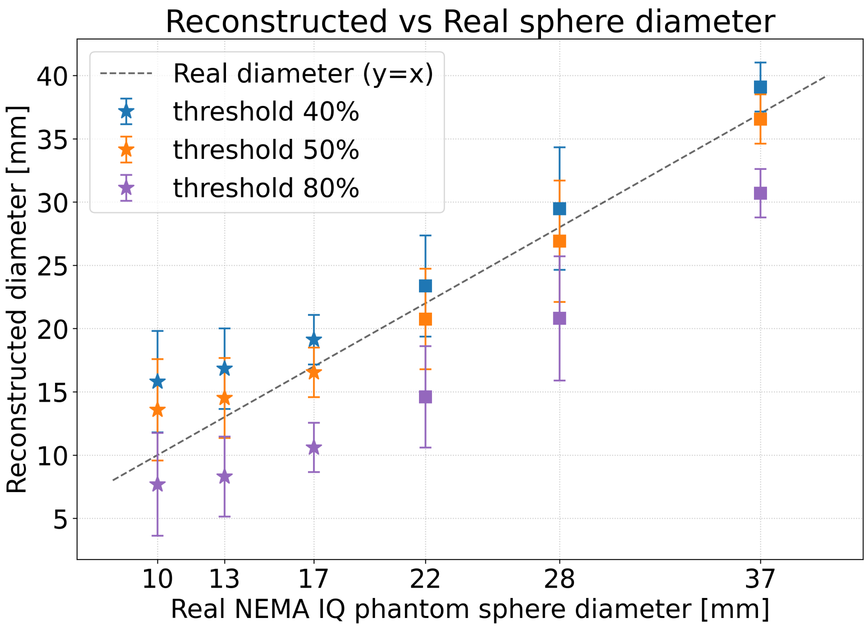

Figure 4.4: Reconstructed diameters from simulated data for ^{44}Sc with the maximum range mode at selected intensity thresholds (40%, 50%, and 80%). Only the first, middle, and last interpretable thresholds are shown for readability; a plot with all thresholds is provided in Appendix Appendix 4.The treshold 100% would mean that only the pixels with 100% of the maximum intensity are taken into account for the diameter reconstruction.

only slight overestimation for ^{44}Sc occurs for the two smallest spheres (10 mm and 13 mm), which are only 4 and 5 pixels in size, respectively. The algorithm, although programmed to interpolate between pixels, is inherently less sensitive for spheres comprising a smaller number of pixels.

Both radioisotopes yielding comparable results for the larger spheres. Ineterestingly, the main difference between the isotopes emerges for the smallest spheres (10 and 13 mm), where ^{44}Sc shows a noticeably larger overestimation (+3.6 mm and +1.5 mm, respectively) compared to ^{18}F (+2.0 mm and -0.1 mm). This is physically expected: the higher-energy positrons of ^{44}Sc produce a broader activity distribution, which shifts the apparent edge outward when combined with Gaussian smoothing. For larger spheres the effect is less pronounced, possibly because spill-out of ^{44}Sc positrons (visible in the histograms below) removes some counts from the sphere interior, partially counteracting the outward edge shift.

Table 4.3: Reconstructed diameters and uncertainties for the ^{18}F-filled spheres at the 40%, 50% and 80% intensity thresholds.

Real diameter	40%	50%	80%
	d ± s(d) (mm)	d ± s(d) (mm)	d ± s(d) (mm)
37	39.8 ± 2.1	37.6 ± 2.1	31.8 ± 2.1
28	29.4 ± 7.0	27.2 ± 7.0	21.5 ± 7.1
22	23.4 ± 4.0	21.2 ± 4.0	15.8 ± 4.0
17	18.4 ± 1.9	16.2 ± 1.9	11.1 ± 2.0
13	15.0 ± 3.2	12.9 ± 3.2	7.8 ± 3.1
10	14.0 ± 4.0	12.0 ± 4.0	6.8 ± 4.1

A similar table was prepared for ^{44}Sc to complete the results for this radioisotope in this section (Table 4.4).

Table 4.4: Reconstructed diameters and uncertainties for the ^{44}Sc-filled spheres at the 40%, 50% and 80% intensity thresholds.

Real diameter	40%	50%	80%
	d ± s(d) (mm)	d ± s(d) (mm)	d ± s(d) (mm)
37	39.1 ± 1.9	36.6 ± 1.9	30.7 ± 1.9
28	29.5 ± 4.8	26.9 ± 4.8	20.8 ± 4.9
22	23.4 ± 4.0	20.8 ± 4.0	14.6 ± 4.0
17	19.1 ± 2.0	16.5 ± 2.0	10.6 ± 2.0
13	16.8 ± 3.2	14.5 ± 3.2	8.3 ± 3.2
10	15.8 ± 4.0	13.6 ± 4.0	7.7 ± 4.1

A closer look at the tables reveals that the reconstructed diameters for both isotopes are very similar across most sphere sizes, with the clearest difference appearing for the smallest spheres (10 and 13 mm), where ^{44}Sc overestimates more than ^{18}F - consistent with the broader positron range of scandium. However, for the three largest spheres (37, 28, and 22 mm) the ^{18}F values are marginally larger than those for ^{44}Sc at the 50% threshold, which is counterintuitive given the shorter positron range of fluorine. This likely results from the competing effects of spill-out and Gaussian smoothing: in the maximum range mode, a fraction of ^{44}Sc positrons escapes the sphere boundary (Figs. 4.5 and 4.6), reducing the count density near the edge and partially offsetting the outward blurring introduced by the Gaussian filter. The net effect is an apparent diameter for ^{44}Sc that is slightly smaller than for ^{18}F in large spheres, even though the true activity distribution is broader. Still, the results yield correct when uncertainty is taken into account, for both radioisotopes.

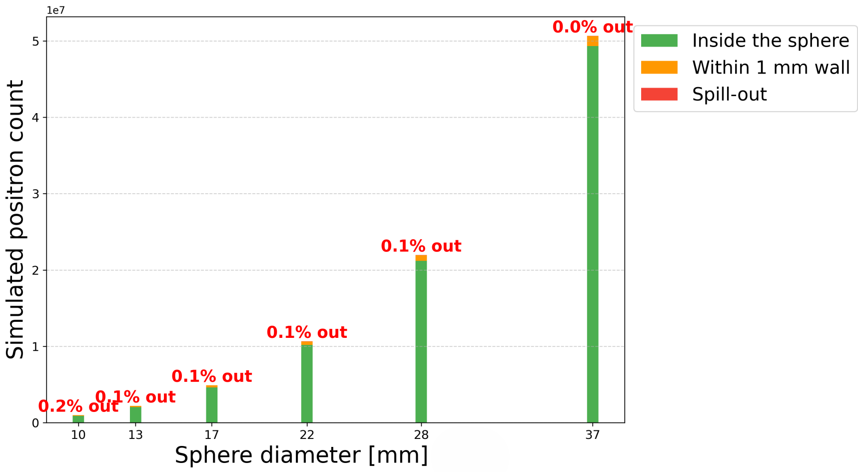

Figure 4.5: Histogram of positron stopping points for ^{18}F. The vast majority of positrons stop inside the water-filled sphere (green) or the plastic wall (orange), with at most 0.2% spilling outside the system.

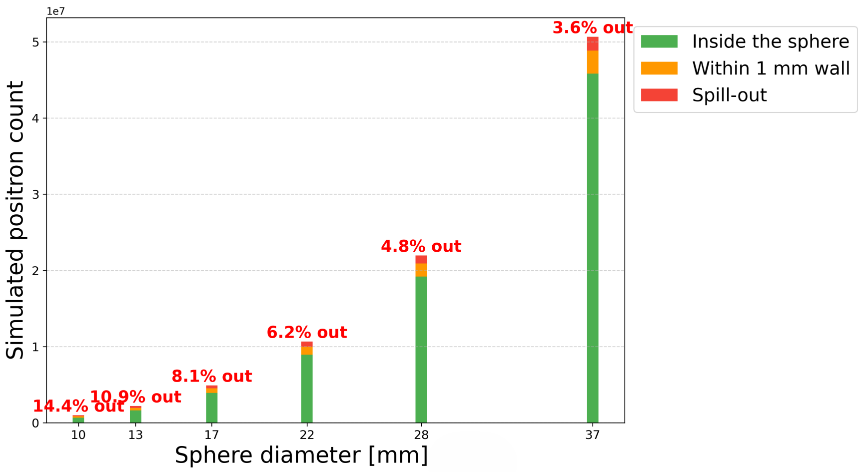

Figure 4.6: Histogram of positron stopping points for ^{44}Sc. A significantly larger fraction of positrons spills outside the system (red), ranging from 14.5% for the 10 mm sphere down to 3.6% for the 37 mm sphere.

4.2.2 Mean Range Mode

The results for the mean range mode (described in detail in Section Monte Carlo Simulation) are presented in Figures 4.7 and 4.8.

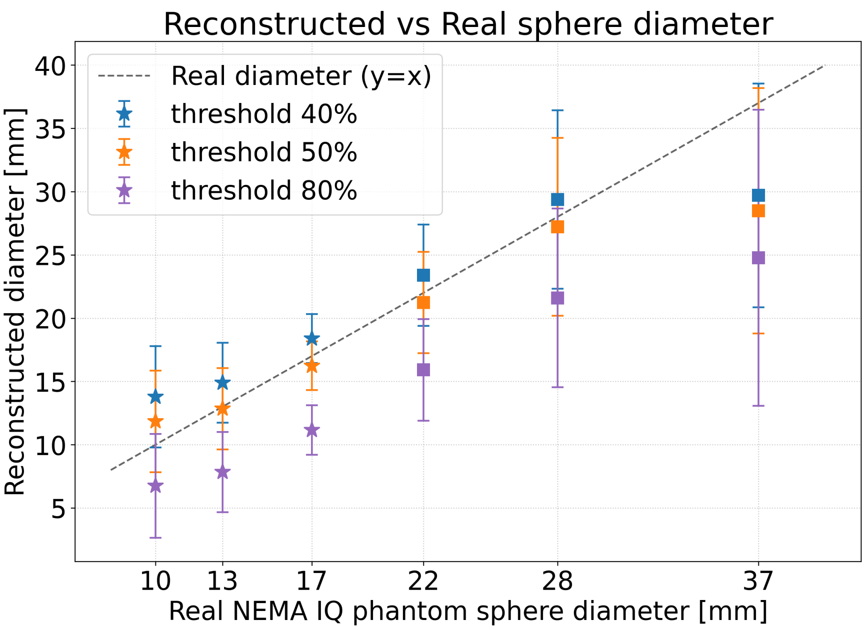

Figure 4.7: Reconstructed diameters from simulated data for ^{18}F with the mean range mode at selected intensity thresholds (40%, 50%, and 80%). The threshold 100% would mean that only the pixels with 100% of the maximum intensity are taken into account for the diameter reconstruction. Only the first, middle, and last interpretable thresholds are shown for readability; a plot with all thresholds is provided in Appendix Appendix 5.

As can be seen, the 50% threshold is the one closest to the real NEMA IQ phantom diameters. Still, the highest and lowest interpretable thresholds (40% and 80%) still fall within the expected values when uncertainty is taken into account. To provide comprehensive results, Tables 4.5 and 4.6 list the exact reconstructed diameters.

Table 4.5: Reconstructed diameters and uncertainties for the ^{18}F-filled spheres at the 40%, 50% and 80% intensity thresholds.

Real diameter (mm)	40%	50%	80%
	d ± s(d) (mm)	d ± s(d) (mm)	d ± s(d) (mm)
37	29.7 ± 8.8	28.5 ± 9.7	24.8 ± 11.7
28	29.4 ± 7.1	27.2 ± 7.0	21.6 ± 7.1
22	23.4 ± 4.0	21.2 ± 4.0	15.9 ± 4.0
17	18.4 ± 1.9	16.2 ± 1.9	11.2 ± 2.0
13	14.9 ± 3.2	12.8 ± 3.2	7.8 ± 3.2
10	13.8 ± 4.0	11.8 ± 4.0	6.8 ± 4.1

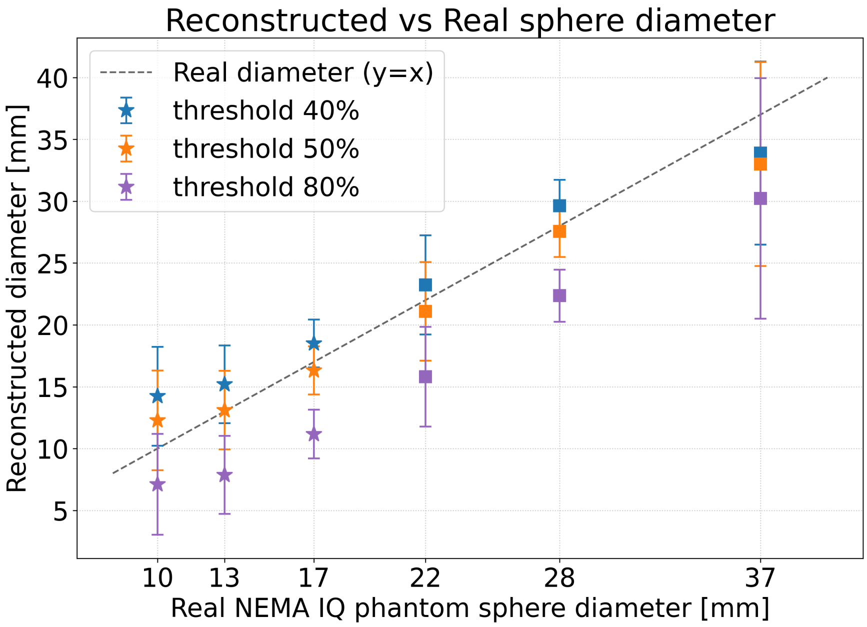

Figure 4.8: Reconstructed diameters from simulated data for ^{44}Sc with the mean range mode at selected intensity thresholds (40%, 50%, and 80%). The threshold 100% would mean that only the pixels with 100% of the maximum intensity are taken into account for the diameter reconstruction. Only the first, middle, and last interpretable thresholds are shown for readability; a plot with all thresholds is provided in Appendix Appendix 5.

Looking at the values for the largest sphere (37 mm) for both radioisotopes, the diameters reconstructed in the mean range mode are slightly lower than the real value (28.5 $\pm$ 9.7 mm for ^{18}F and 33.0 $\pm$ 8.2 mm for ^{44}Sc at the 50% threshold), though the differences are within the measurement uncertainties. A plausible explanation is that the Gaussian smoothing shifts the intensity profiles inward. Unlike in the maximum range mode, where the 37 mm sphere was reconstructed accurately, here the calculated positron range is shorter (mean of interactions inside matter, as opposed to the maximum straight-line range), so the activity distribution is narrower. Consequently, the relative effect of Gaussian smoothing on the apparent edge is more pronounced, causing a slight inward shift of the reconstructed boundary for both isotopes.

Notably, the reconstructed diameters for ^{44}Sc are now generally larger than for ^{18}F - most clearly for the 37 mm sphere (33.0 mm vs.$\tilde{2}$8.5 mm at the 50% threshold). This is the physically expected trend, as the higher positron energy of ^{44}Sc produces a broader activity distribution. The fact that this pattern was not clearly visible in the maximum range mode supports the interpretation that spill-out effects (present in the maximum but not the mean range mode) partially mask the influence of positron range on the reconstructed image. In the mean range mode, where no activity is lost to spill-out (Figs. 4.9 and 4.10), the smoothing-induced edge displacement is the dominant effect, and the expected isotope-dependent difference becomes apparent.

To confirm that the positron range in this mode is indeed smaller and to examine

Table 4.6: Reconstructed diameters and uncertainties for the ^{44}Sc-filled spheres at the 40%, 50% and 80% intensity thresholds.

Real diameter (mm)	40%	50%	80%
	d ± s(d) (mm)	d ± s(d) (mm)	d ± s(d) (mm)
37	33.9 ± 7.4	33.0 ± 8.2	30.2 ± 9.7
28	29.6 ± 2.1	27.6 ± 2.1	22.4 ± 2.1
22	23.2 ± 4.0	21.1 ± 4.0	15.8 ± 4.0
17	18.5 ± 1.9	16.3 ± 1.9	11.2 ± 2.0
13	15.2 ± 3.1	13.1 ± 3.2	7.9 ± 3.2
10	14.2 ± 4.0	12.3 ± 4.0	7.1 ± 4.1

the effect of Gaussian smoothing, histograms of stopping positions were prepared (Figures 4.9 and 4.10). The data confirm that before smoothing, all positrons stopped within the spheres or the plastic boundary, with no spill-out for either isotope (0.0% in all cases). This is expected, as the mean range mode calculates a shorter path length than the maximum range mode, so virtually all positrons are contained within the phantom geometry. Since no activity is lost outside the spheres, the underestimation observed for the 37 mm sphere can be attributed solely to the smoothing of intensity profiles, without the confounding effect of signal loss to the surroundings.

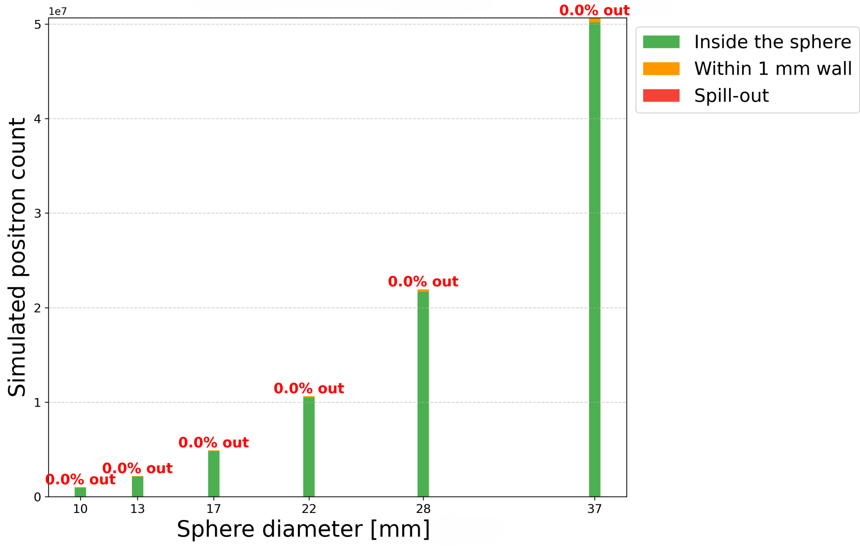

Figure 4.9: Histogram of positron stopping points for ^{18}F in the mean range mode. All positrons stop inside the water-filled sphere (green) or the plastic wall (orange); no spill-out is observed (0.0% out for all sphere sizes).

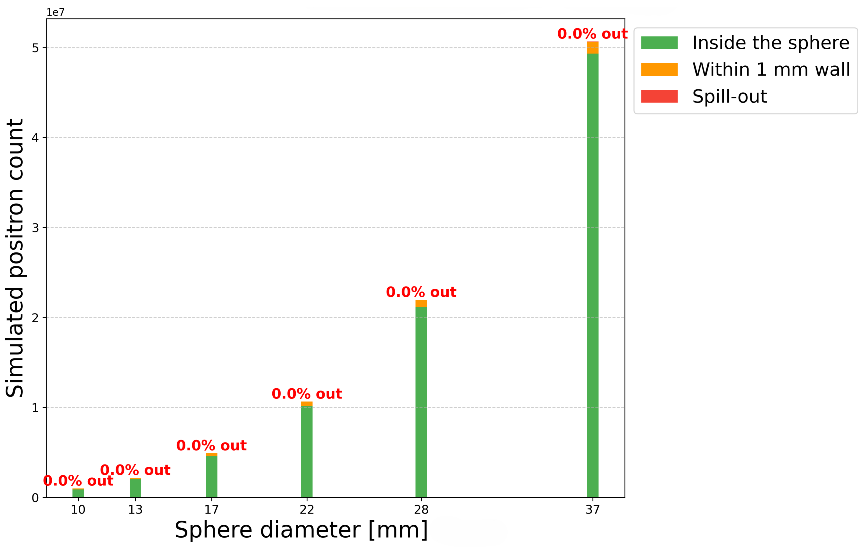

Figure 4.10: Histogram of positron stopping points for ^{44}Sc in the mean range mode. Similarly to ^{18}F, no positrons spill outside the system (0.0% out for all sphere sizes), confirming that the shorter calculated range in this mode fully contains the activity within the phantom.

5 Discussion of the Results

Comparing the results from the two positron range calculation modes (maximum and mean range), the reconstructed diameters are generally consistent within their uncertainties, although some differences emerge for the largest sphere. For ^{18}F at the 50% threshold, the maximum range mode reconstructs the 37 mm sphere accurately (37.6 $\pm$ 2.1 mm), while the mean range mode underestimates it (28.5 $\pm$ 9.7 mm) - though the large uncertainty makes the difference less conclusive. For ^{44}Sc, both modes yield similar results at the 50% threshold (36.6 $\pm$ 1.9 mm vs. 33.0 $\pm$ 8.2 mm). In both cases, the 50% threshold gives the most accurate results for the two radioisotopes. Although the stopping point histograms show a clear difference for ^{44}Sc in the maximum range mode (up to 14.5% spill-out for the smallest sphere), and are well aligned with theory for the mean range mode (both isotopes) and the maximum range mode for ^{18}F (negligible spill-out), this difference is partially masked after image reconstruction and Gaussian smoothing. The spill-out visible in the histograms does affect the reconstructed diameters - for example, the 37 mm sphere for ^{44}Sc is larger in the maximum than in the mean range mode (36.6 vs. 33.0 mm) - but the effect is comparable to or smaller than the reconstruction uncertainties. It should also be noted that the simulation was a TOY Monte Carlo - a pilot study for this effect - and it is plausible that professional Monte Carlo codes such as PHITS, PENELOPE or GEANT-4 would yield more quantitatively accurate results.

To put the simulation performance into a broader perspective, Table 5.1 compares the reconstructed diameters for two representative spheres - the 17 mm sphere filled with ^{18}F and the 22 mm sphere filled with ^{44}Sc - across all three thresholds, for both experimental data and the two simulation modes. An interesting pattern can be observed. For the ^{18}F-filled sphere, the two simulation modes produce nearly identical results at every threshold (e.g., 18.4 $\pm$ 1.9 mm vs. 18.4 $\pm$ 1.9 mm at 40%), and both overestimate the true diameter by roughly 1-3 mm. The experimental values, however, are systematically lower (15.6 $\pm$ 2.7 mm at 40%), suggesting that additional blurring effects present in the real measurement - such as finite detector resolution, scatter, and imperfect calibration - reduce the apparent sphere size beyond what the simulation captures.

The picture changes for the ^{44}Sc-filled sphere, where the positron range effect is expected to be dominant. At the 40% threshold, the experimental diameter reaches 33.3 $\pm$ 5.7 mm - far above the true 22 mm, and roughly 10 mm larger than either simulation mode (23 mm). This is precisely the signature of positron range spill-out: higher-energy ^{44}Sc positrons travel farther before annihilating, and at a 40% threshold the reconstructed sphere appears artificially inflated. The simulation captures the qualitative direction of this effect (both MC modes yield slightly higher values than the ^{18}F case at the same threshold), but severely

Table 5.1: Comparison of real NEMA IQ phantom sphere diameters (17 mm and 22 mm) vs. reconstructed values. Results are presented as d ± s(d) (mm).

Sphere & Isotope	Threshold	Data Source (Diameter in mm)		
		Experiment	MC Max Range	MC Mean Range
17 mm (Fluorine)	40%	15.6 ± 2.7	18.4 ± 1.9	18.4 ± 1.9
	50%	13.4 ± 2.7	16.2 ± 1.9	16.2 ± 1.9
	80%	8.0 ± 2.9	11.1 ± 2.0	11.2 ± 2.0
22 mm (Scandium)	40%	33.3 ± 5.7	23.4 ± 4.0	23.2 ± 4.0
	50%	24.9 ± 3.0	20.8 ± 4.0	16.2 ± 1.9
	80%	15.4 ± 2.8	14.6 ± 4.0	15.8 ± 4.0

underestimates its magnitude. At 50%, the experimental value (24.9 ± 29.8 mm) carries a high uncertainty, indicating that the measurement becomes unstable at this threshold for the smaller sphere with the more energetic isotope. The simulation modes diverge here as well: the maximum range model gives 20.8 ± 4.0 mm, while the mean range model drops to 16.2 ± 1.9 mm - a 4.5 mm gap that reflects the same sensitivity of the mean range model to threshold choice observed for the larger spheres. At 80%, all three sources converge to roughly 15 mm, though this convergence reflects the fact that aggressive thresholding strips away most of the sphere volume regardless of the positron range.

Turning to the experimental results more broadly, the experiment confirmed the hypothesis that positron range - a function of positron energy and thus closely related to the choice of radioisotope - has a measurable impact on image reconstruction. ^{44}Sc has a broader energy spectrum than ^{18}F, producing higher-energy positrons that smear the reconstructed image; this effect is clearly observable on the Modular J-PET tomograph. At the 50% threshold the ^{44}Sc-filled spheres are systematically overestimated, while the ^{18}F results are consistent with the literature [4]. This overestimation indicates that the simulations underestimate the positron range effect relative to the experiment - a discrepancy that has been reported before by Carter et al. [5]. Six radioisotopes were studied with mean positron energies from 242 keV (^{52}Mn) to 1170 keV (^{72}As), a range within which ^{44}Sc (mean energy 632 keV) fits near the middle, as shown in Fig. 5.1.

Carter et al. found that their PHITS simulations systematically underestimated the blurring effect of positron range relative to PET images of the Jaszczak phantom. As they conclude, for positron emitters more energetic than ^{89}Zr (mean energy 396 keV) - which includes ^{44}Sc - image quality and quantitative accuracy for small structures degrades rapidly. Therefore, the experimental findings of the present study are consistent with the literature, and the observed discrepancy between simulation and experimental reconstruction is not unique to the TOY Monte Carlo approach; even more complex simulation programs exhibit the same underestimation of positron range effects.

Taken together, the results in Table 5.1 reinforce the central conclusion: while the

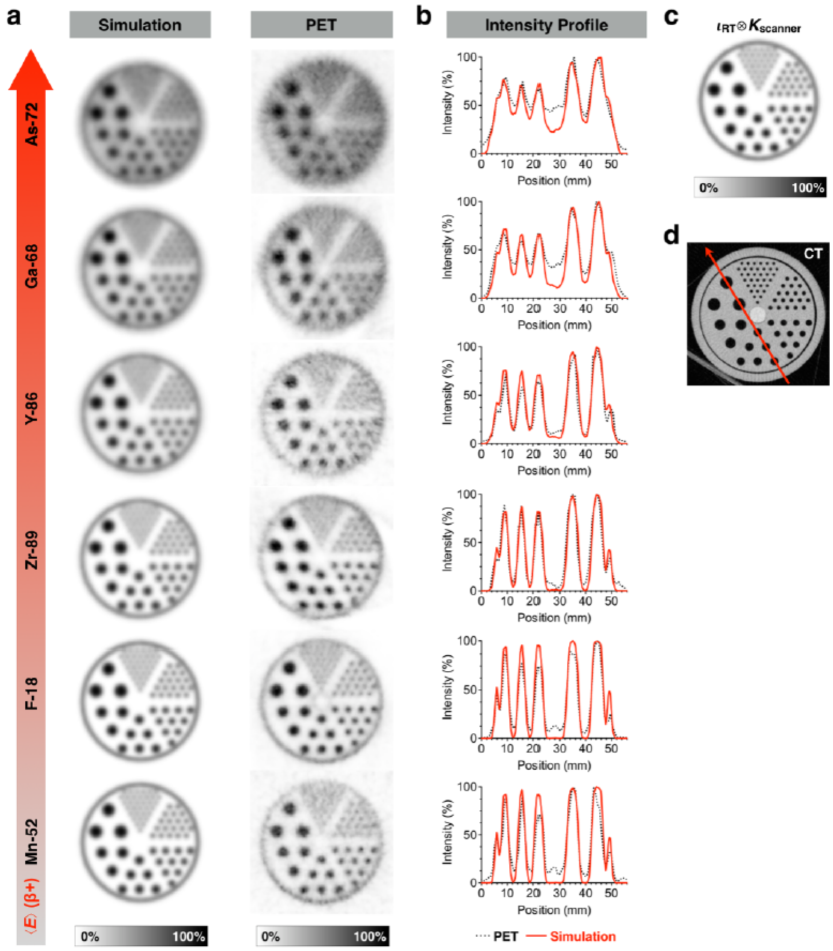

Figure 5.1: Comparison of PET images and PHITS simulations of the Jaszczak phantom for six positron emitters (adapted from Carter et al. [5]). Panel (a): side-by-side comparison of reconstructed images from simulation (left row) and PET (right row), ordered by increasing mean positron energy. Panel (b): intensity profiles along the line indicated in panel (d), comparing PET (dotted line) with simulation (solid red line). Panel (c): the simulated ground truth radiotracer distribution convolved with the scanner PSF, representing the upper bound on achievable resolution. Panel (d): CT reference scan of the phantom with the profile line marked.

TOY Monte Carlo simulation captures the qualitative trend of positron range differences between ^{18}F and ^{44}Sc, only the experimental data - owing to the inherently more complete physics of the measurement - reveal the full magnitude of the effect. The simulations reproduce the two isotopes' relative ordering but miss the absolute scale of the spill-out, particularly for ^{44}Sc at generous thresholds. This underscores the importance of experimental validation for any simulation-based study of positron range, particularly for higher-energy emitters where the effect is most pronounced. Perhaps, due to its high energy, ^{68}Ga would be the best candidate for further investigation and quantification of the effect of positron range on PET imaging.

6 Summary and Conclusions

In this study the implications of choosing ^{18}F and ^{44}Sc on PET image resolution, by comparing data obtained from experiment and from an in-house Monte Carlo simulation was investigated. Specifically, the diameters of NEMA IQ phantom spheres from NIfTI files were estimated - for the experimental data and self-produced for the simulations.

For this purpose, an in-house Monte Carlo simulation was developed that modelled the maximum and mean positron range for two radioisotopes (^{44}Sc and ^{18}F) in the NEMA IQ phantom. The simulated data were then reconstructed and the sphere diameters were determined. The main findings showed that the maximum range model gave substantially better results than the mean range model. For the 37 mm sphere filled with ^{18}F and evaluated at the 50% threshold, the maximum range model recovered 37.6 ± 2.1 mm, very close to the true diameter, whereas the mean range model yielded 28.5 ± 9.7 mm — an underestimation of nearly 9 mm with over four times larger uncertainty. Nevertheless, when uncertainty was included, all results contained the true sphere diameter, especially at the 50% threshold. At the 40% and 80% thresholds in the maximum range mode, the recovered diameters were respectively larger and smaller than the true values, as expected from the thresholding bias.

The mean range mode proved to be more error-prone. It is likely due to the applied Gaussian Smoothing that blurred the boundaries inward, which resulted in virtually smaller spheres, than in reality. The effect is not visible for the maximum range model, most likely accounting to the bigger positron ranges that evened out this effect.

The simulation results, however, did not convey to the experimental results. Data from the experiment were - from the point of NIfTI file - reconstructed by the same code as the simulated data. Yet, the experimental results revealed substantial effect for the spheres filled with ^{44}Sc - that the higher threshold (so fewer pixels) yield best results, suggesting a considerable spill-out accounting for the positron range. For ^{18}F, which is less energetic, the results proved to be in line with results presented in different papers that taking 50% threshold reflects well on the real spheres' diameters, when uncertainty is taken into acocunt. Although, my results suggested that taking smaller threshold (so more pixels) would prove to be more effective yet. Possibly, the reson for this is the limited spatial resolution of the detector for smaller spheres - as sphere of the 10 mm dimatere is only 4 voxels/pixels in size, meaning the least trustable results.

Overall, the results suggest that there is an impact on image quality in ^{44}Sc PET imaging, which should be accounted for in the reconstruction phase. The effect was not quantified, nor the simulations managed to capture it - which is in line with results of other researchers [5]. The next step in this research would be to prepare a more complex Monte Carlo simulation in one of the established programms like PHITS, GEANT-4 or

PENELOPE, and try to capture the effect of positron range there, to then incorporate corrections in positron emission tomographs that account on the isotope (and its energy) used during the imaging procedure, to enhance the spatial resolution of this imiging method.

Bibliography

[1] Stefaan Vandenberghe, Pawel Moskal, and Joel S Karp. State of the art in total body pet. *EJNMMI physics*, 7(1):35, 2020.

[2] Paweł Moskal and Ewa Stępień. Prospects and clinical perspectives of total-body pet imaging using plastic scintillators. *PET clinics*, 15(4):439–452, 2020.

[3] Luca Filippi and Roberta Danieli. Unlocking the brain's secrets: the neuroexplorer revolution in pet imaging. *Expert Review of Medical Devices*, 22(8):783–786, 2025. PMID: 40530816.

[4] Craig S Levin and Edward J Hoffman. Calculation of positron range and its effect on the fundamental limit of positron emission tomography system spatial resolution. *Physics in Medicine & Biology*, 44(3):781–799, 1999.

[5] L. M. Carter, Adam Leon Kesner, E. C. Pratt, V. A. Sanders, A. V. F. Massicano, C. S. Cutler, S. E. Lapi, and Jason S. Lewis. The impact of positron range on pet resolution, evaluated with phantoms and phits monte carlo simulations for conventional and non-conventional radionuclides. *Molecular Imaging and Biology*, 22(1):73–84, 2020.

[6] Lars Jødal, Cindy Le Loirec, and Christophe Champion. Positron range in pet imaging: an alternative approach for assessing and correcting the blurring. *Physics in medicine and biology*, 57(12):3931–3943, 2012.

[7] Pro-Project Group Sp. z o.o. Pronm nema nu2 - diagnomatic. `https://www.diagnomatic.com/pl/devices/pro-nm-nema-nu2`, 2026. Dostęp: 2026-06-24.

[8] Terry Jones and David Townsend. History and future technical innovation in positron emission tomography. *Journal of Medical Imaging*, 4(1):011013–011013, 2017.

[9] CERN. Discovering the positron, 2019.

[10] Andrea Gallamini, Colette Zwarthoed, and Anna Borra. Positron emission tomography (pet) in oncology. *Cancers*, 6(4):1821–1889, 2014.

[11] Simon R Cherry, Terry Jones, Joel S Karp, Jinyi Qi, William W Moses, and Ramsey D Badawi. Total-body pet: maximizing sensitivity to create new opportunities for clinical research and patient care. *Journal of Nuclear Medicine*, 59(1):3–12, 2018.

[12] Michael Charlton and John Watkin Humberston. *Positron Physics*, volume 11 of *Cambridge Monographs on Atomic, Molecular and Chemical Physics*. Cambridge University Press, Cambridge, 2001.

[13] Paweł Moskal, Jakub Baran, Steven Bass, Jarosław Choiński, Neha Chug, Catalina Curceanu, Eryk Czerwiński, Meysam Dadgar, Manish Das, Kamil Dulski, et al. Positronium image of the human brain in vivo. *Science Advances*, 10(37):eadp2840, 2024.

[14] Saira Shaik, Malathi Mulaparthi, Haveela V, Harthika Sk, Durga D, and Krishna V. A review on the positron emission tomography radiotracers: Review article. *Journal of Pharma Insights and Research*, 3:286–292, 10 2025.

[15] Qwerty123uiop. Photomultiplier tube schematic. `https://commons.wikimedia.org/w/index.php?curid=62426194`. Licencja: CC BY-SA 3.0.

[16] Charles L Melcher. Scintillation crystals for pet. *Journal of Nuclear Medicine*, 41(6):1051–1055, 2000.

[17] Shan Tong, Adam M Alessio, and Paul E Kinahan. Image reconstruction for pet/ct scanners: past achievements and future challenges. *Imaging in medicine*, 2(5):529, 2010.

[18] Manish Das, Reimund Bayerlein, Sushil Sharma, Szymon Parzych, Szymon Niedźwiecki, Ramsey Badawi, Ermias Yitayew Beyene, Neha Chug, Catalina Curceanu, Eryk Czerwiński, et al. Development of correction techniques for the j-pet scanner. 2024.

[19] Edward J. Hoffman, Sung-Cheng Huang, Michael E. Phelps, and David E. Kuhl. Quantitation in positron emission computed tomography: 4. effect of accidental coincidences. *Journal of Computer Assisted Tomography*, 5(3):391–400, 1981.

[20] Szymon Niedźwiecki, Piotr Białas, Catalina Curceanu, Eryk Czerwiński, Kamil Dulski, Alexsander Gajos, Bartosz Głowacz, M Gorgol, BC Hiesmayr, B Jasińska, et al. J-pet: a new technology for the whole-body pet imaging. *arXiv preprint arXiv:1710.11369*, 2017.

[21] Pawel Moskal, Daria Kisielewska, Catalina Curceanu, Eryk Czerwiński, Kamil Dulski, Aleksander Gajos, Marek Gorgol, B Hiesmayr, B Jasińska, Krzysztof Kacprzak, et al. Feasibility study of the positronium imaging with the j-pet tomograph. *Physics in Medicine & Biology*, 64(5):055017, 2019.

[22] AL Nichols. Decay data:: review of measurements, evaluations and compilations. *Applied radiation and isotopes*, 55(1):23–70, 2001.

[23] NuDoubt++ Collaboration. Understanding double beta decay. `https://nudoubt.uni-mainz.de/public.php`. Dostęp: 11.06.2026.

[24] NuPECC. *Nuclear Physics for Medicine*. European Science Foundation, 2014. Dostęp: 2026-05-20.

[25] Saira Bhanu Shaik, Malathi Mulaparthi, Haveela V, Harthika Shaharin Sk, Durga Bhavani D, and Krishna Murthy V. A review on the positron emission tomography radiotracers. *Journal of Pharma Insights and Research*, 3(5):286–292, Oct 2025.

[26] Cristina Müller, Katharina A Domnanich, Christoph A Umbricht, and Nicholas P van der Meulen. Scandium and terbium radionuclides for radiotheranostics: current state of development towards clinical application. *The British journal of radiology*, 91(1091):20180074, 2018.

[27] Maurizio Conti and Lars Eriksson. Physics of pure and non-pure positron emitters for PET: a review and a discussion. *EJNMMI Physics*, 3(1):8, 2016.

[28] IMV Medical Information Division. Imv pet scan volumes continue to grow. `https://www.scienceandmedicinegroup.com/resource/imv-pet-scan-volumes-continue-to-grow/`, 2023. Science and Medicine Group. Accessed: 2026-05-31.

[29] Paweł Moskal, Kamil Dulski, Neha Chug, Catalina Curceanu, Eryk Czerwiński, Meysam Dadgar, Jan Gajewski, Aleksander Gajos, Grzegorz Grudzień, Beatrix C Hiesmayr, et al. Positronium imaging with the novel multiphoton pet scanner. *Science advances*, 7(42):eabh4394, 2021.

[30] Manish Das, Sushil Sharma, Ermias Yitayew Beyene, Aleksander Bilewicz, Jaroslaw Choinski, Neha Chug, Catalina Curceanu, Eryk Czerwinski, Kavya Valsan Eliyan, Jakub Hajduga, et al. First positronium imaging using 44 sc with the j-pet scanner: a case study on the nema-image quality phantom. *IEEE Transactions on Radiation and Plasma Medical Sciences*, 2025.

[31] C Champion and C Le Loirec. Positron follow-up in liquid water: II. Spatial and energetic study for the most important radioisotopes used in pet. *Physics in Medicine & Biology*, 52(22):6605, oct 2007.

[32] Florian Rosar, Hans-Georg Buchholz, Sebastian Michels, Manuela A Hoffmann, Markus Piel, Christopher M Waldmann, Frank Rösch, Stefan Reuss, and Mathias Schreckenberger. Image quality analysis of 44sc on two preclinical pet scanners: A comparison to 68ga. *EJNMMI physics*, 7(1):16, 2020.

[33] Katharina Domnanich, Cristina Müller, Renata Farkas, Raffaella Schmid, Bernard Ponsard, Roger Schibli, Andreas Türler, and Nicholas van der Meulen. 44sc for labeling of dota- and nodaga-functionalized peptides: preclinical in vitro and in vivo investigations. *EJNMMI Radiopharmacy and Chemistry*, 1, 05 2016.

[34] ZH Cho, JK Chan, L Ericksson, M Singh, S Graham, NS MacDonald, and Y Yano. Positron ranges obtained from biomedically important positron-emitting radionuclides. *Journal of nuclear medicine*, 16(12):1174–1176, 1975.

[35] M Partridge, A Spinelli, W Ryder, and C Hindorf. The effect of $\beta+$ energy on performance of a small animal pet camera. *Nuclear Instruments and Methods in Physics Research Section A: Accelerators, Spectrometers, Detectors and Associated Equipment*, 568(2):933–936, 2006.

[36] Wiktor Mryka, Manish Das, Ermias Yitayew, Pawel Moskal, and Ewa Stepien. Estimating influence of positron range in proton-therapy-beam monitoring with pet. *Bio-Algorithms and Med-Systems*, 19:96–100, 12 2023.

[37] Faranak Tayefi Ardebili, Szymon Niedźwiecki, and Paweł Moskal. Evaluation of modular j-pet sensitivity. 2023.

[38] Szymon Parzych. Optimization of positronium imaging performance of simulated modular j-pet scanner using gate software. *Bio-Algorithms and Med-Systems*, 19(1):80–86, 2023.

[39] Anna Giebułtowska. Praca-licencjacka - repozytorium kodu, 2026. Dostęp: 24.06.2026.

[40] Monika Pawlik-Niedźwiecka. *Determination of performance characteristics of the J-PET tomograph*. PhD thesis, Uniwersytet Jagielloński, 2023.

[41] Chien-Shiung Wu and Steven A. Moszkowski. *Beta Decay*. Interscience Publishers, New York, 1966.

[42] W.F. Slot, G.H. Dulfer, H. Van Der Molen, and H. Verheul. The decay of 6831ga37. *Nuclear Physics A*, 186(1):28–32, 1972.

[43] PRISMAP Consortium. ^{44}Sc (Scandium) – Radionuclide Portfolio. `https://www.prismap.eu/radionuclides/portfolio/44Sc/`, 2021. Dostęp: 2026-06-17.

[44] Hossein Arabi and Habib Zaidi. Improvement of image quality in pet using post-reconstruction hybrid spatial-frequency domain filtering. *Physics in Medicine & Biology*, 63(21):215010, oct 2018.

[45] Joint Committee for Guides in Metrology (JCGM). Evaluation of measurement data – guide to the expression of uncertainty in measurement – part 1: Introduction. Technical Report JCGM GUM-1:2023, Bureau International des Poids et Mesures (BIPM), 2023. Dostęp: 2026-05-23.

Appendix 1

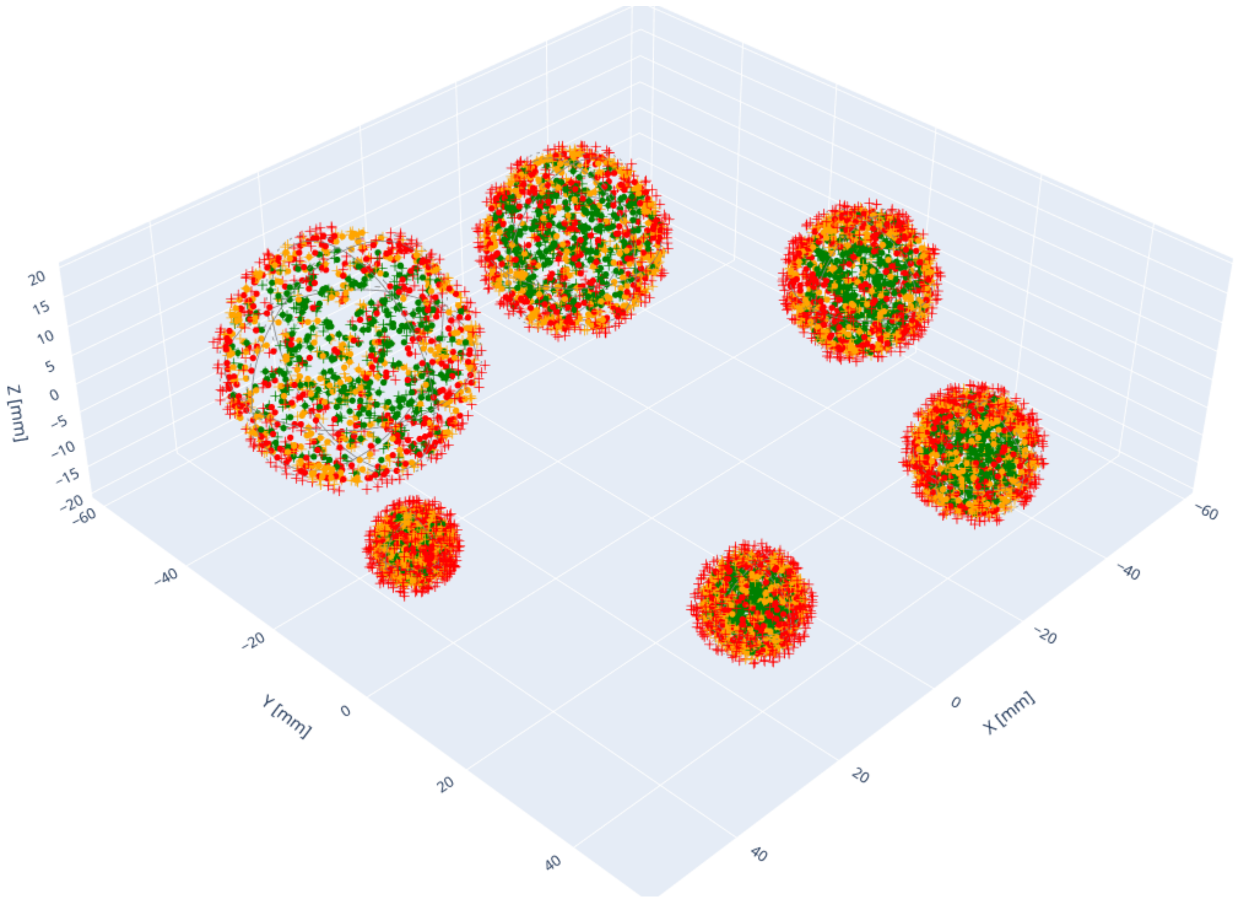

Figure 1: 3D Visualization of stopping points for ^{18}F from simulated data with the maximum positron range mode. Circles denote the starting points, while crosses denote the annihilation points of positrons. In red are the positrons that have escaped the boundaries of the spheres. In yellow are the positrons that stopped within the boundary material, and in green the positrons that have never left the inside of the sphere. Since it was not viable to retrive such an image for all the simulated positrons, only 300 for each sphere were randomly chose to produce this visualization.

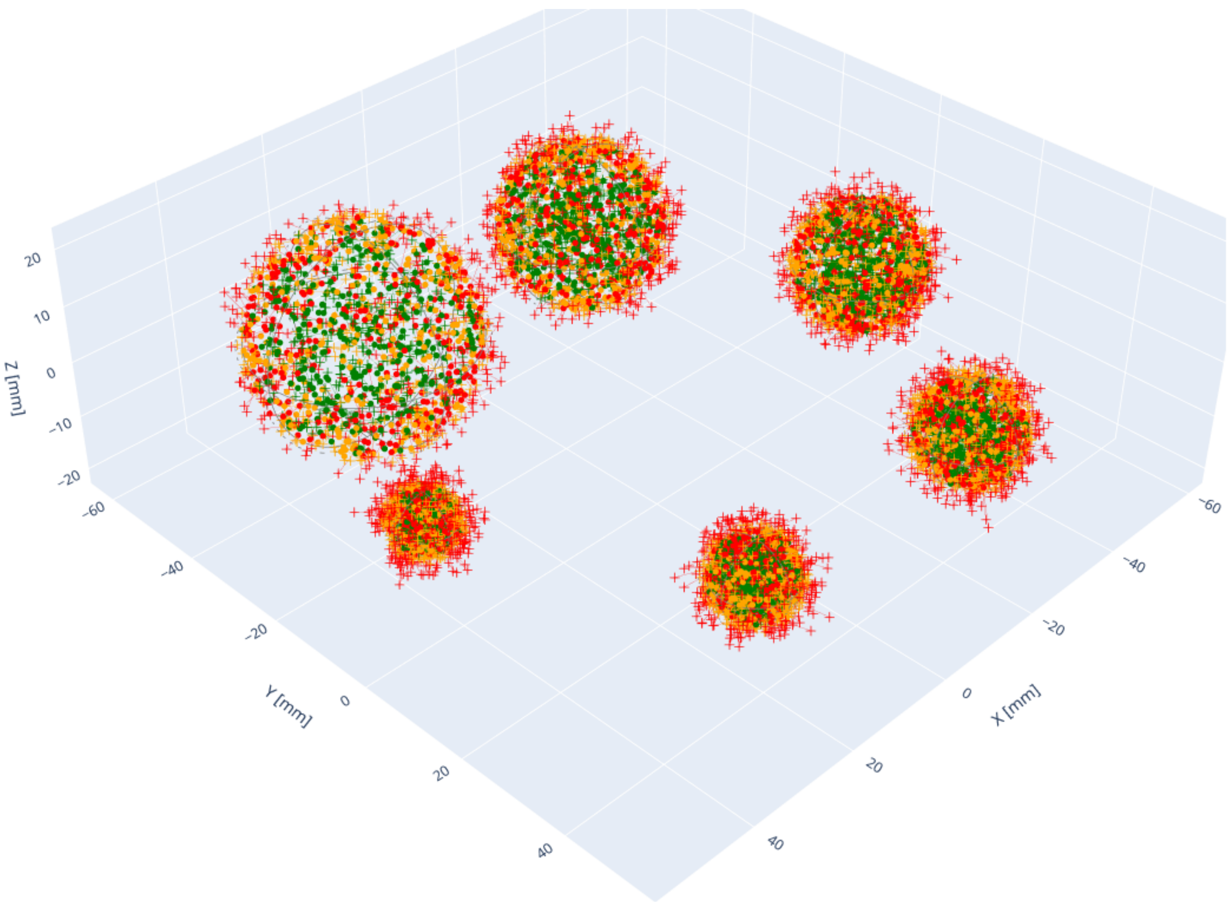

Figure 2: 3D Visualization of stopping points for ^{44}Sc from simulated data with the maximum positron range mode. Circles denote the starting points, while crosses denote the annihilation points of positrons. In red are the positrons that have escaped the boundaries of the spheres. In yellow are the positrons that stopped within the boundary material, and in green the positrons that have never left the inside of the sphere. Since it was not viable to retrive such an image for all the simulated positrons, only 300 for each sphere were randomly chose to produce this visualization.

Appendix 2

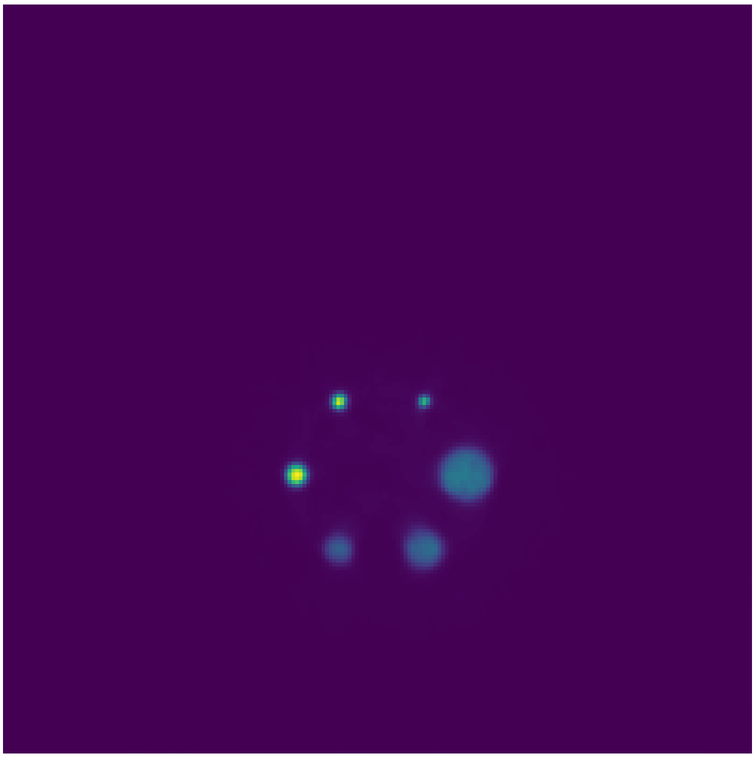

Figure 3: Maximum intensity slice along the z axis obtained from a NIfTI file with experimental data. Three smaller spheres were filled with ^{18}F, while three larger spheres with ^{44}Sc. The brighter the region, the higher activity it had. The slice is the 99th plane from 200 planes in the matrix of the NIfTI file.

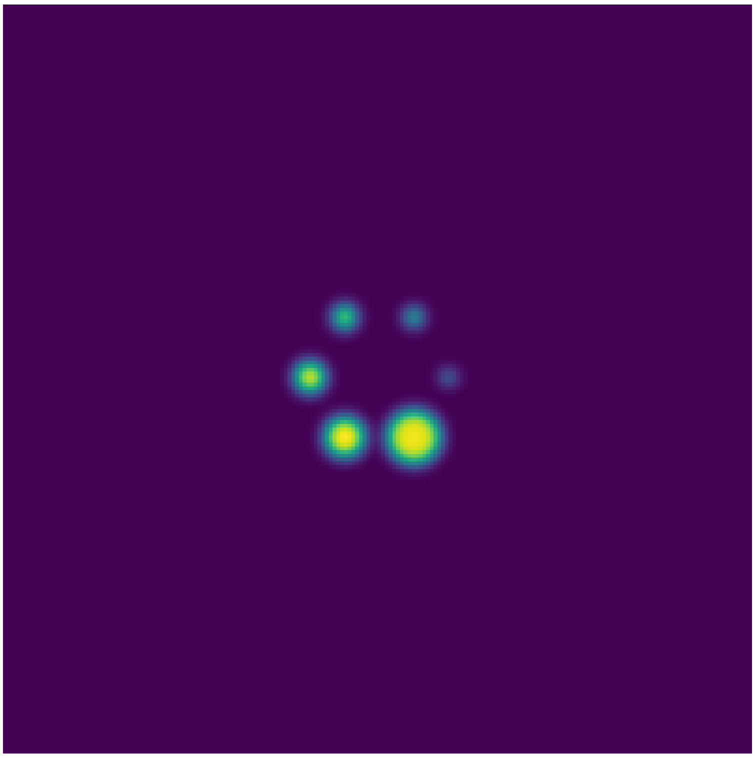

Figure 4: Maximum intensity slice along the z axis obtained from a NIfTI file with simulated data for ^{18}F in the maximum range mode. The brighter the region, the higher activity it had. The slice is the 101st plane from 200 planes in the matrix of the NIfTI file.

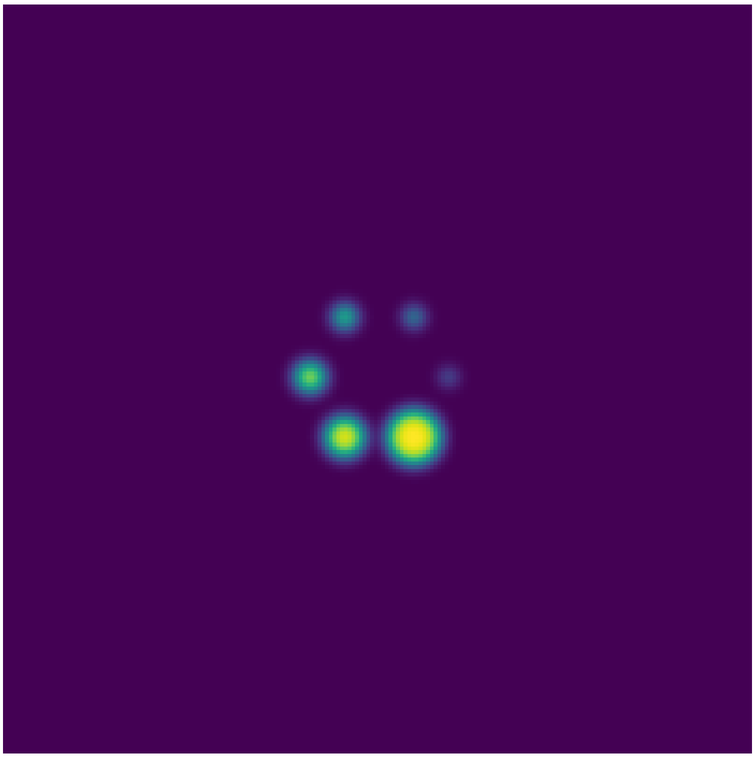

Figure 5: Maximum intensity slice along the z axis obtained from a NIfTI file with simulated data for ^{44}Sc in the maximum range mode. The brighter the region, the higher activity it had. The slice is the 101st plane from 200 planes in the matrix of the NIfTI file.

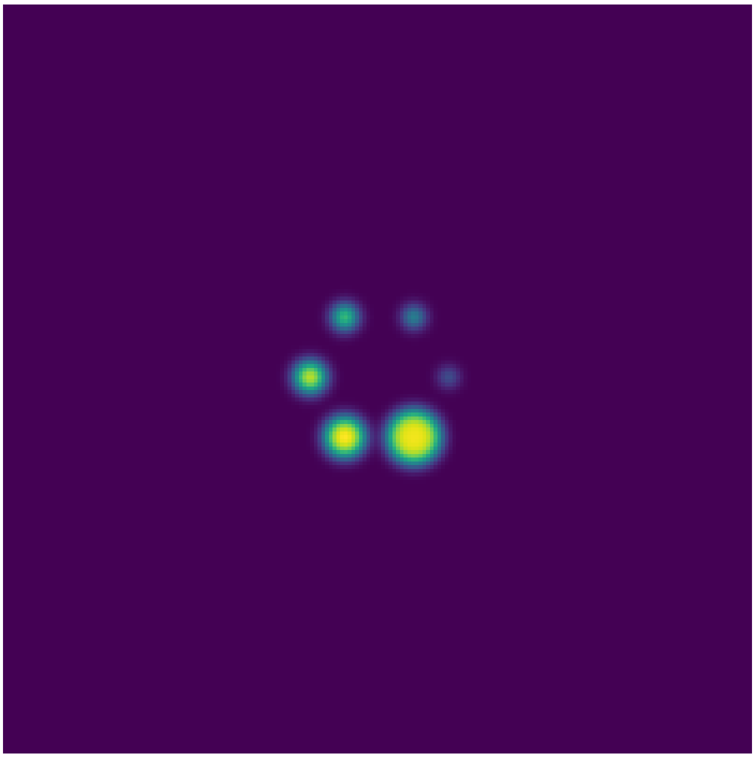

Figure 6: Maximum intensity slice along the z axis obtained from a NIfTI file with simulated data for ^{18}F in the mean range mode. The brighter the region, the higher activity it had. The slice is the 101st plane from 200 planes in the matrix of the NIfTI file.

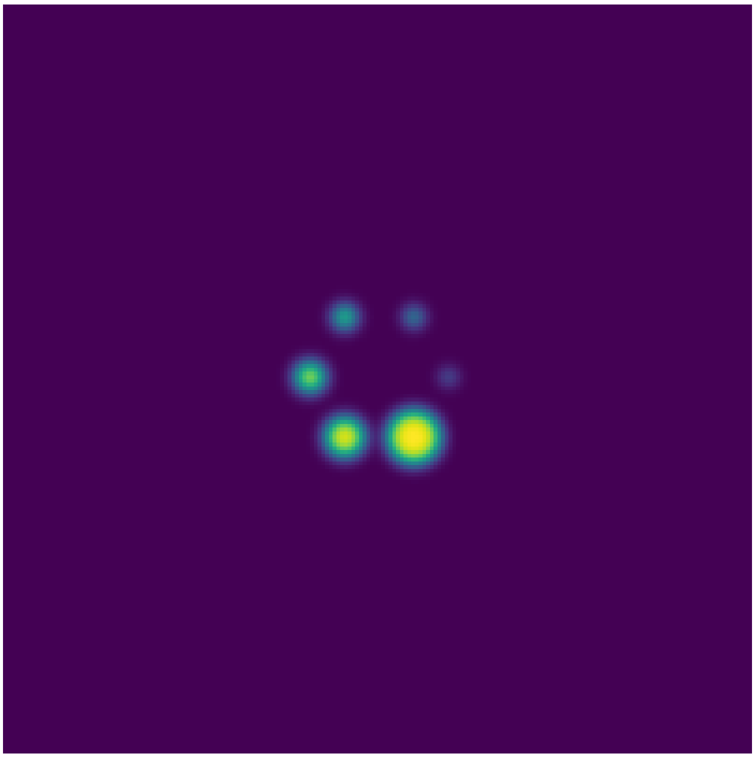

Figure 7: Maximum intensity slice along the z axis obtained from a NIfTI file with simulated data for ^{44}Sc in the mean range mode. The brighter the region, the higher activity it had. The slice is the 101st plane from 200 planes in the matrix of the NIfTI file.

Appendix 3

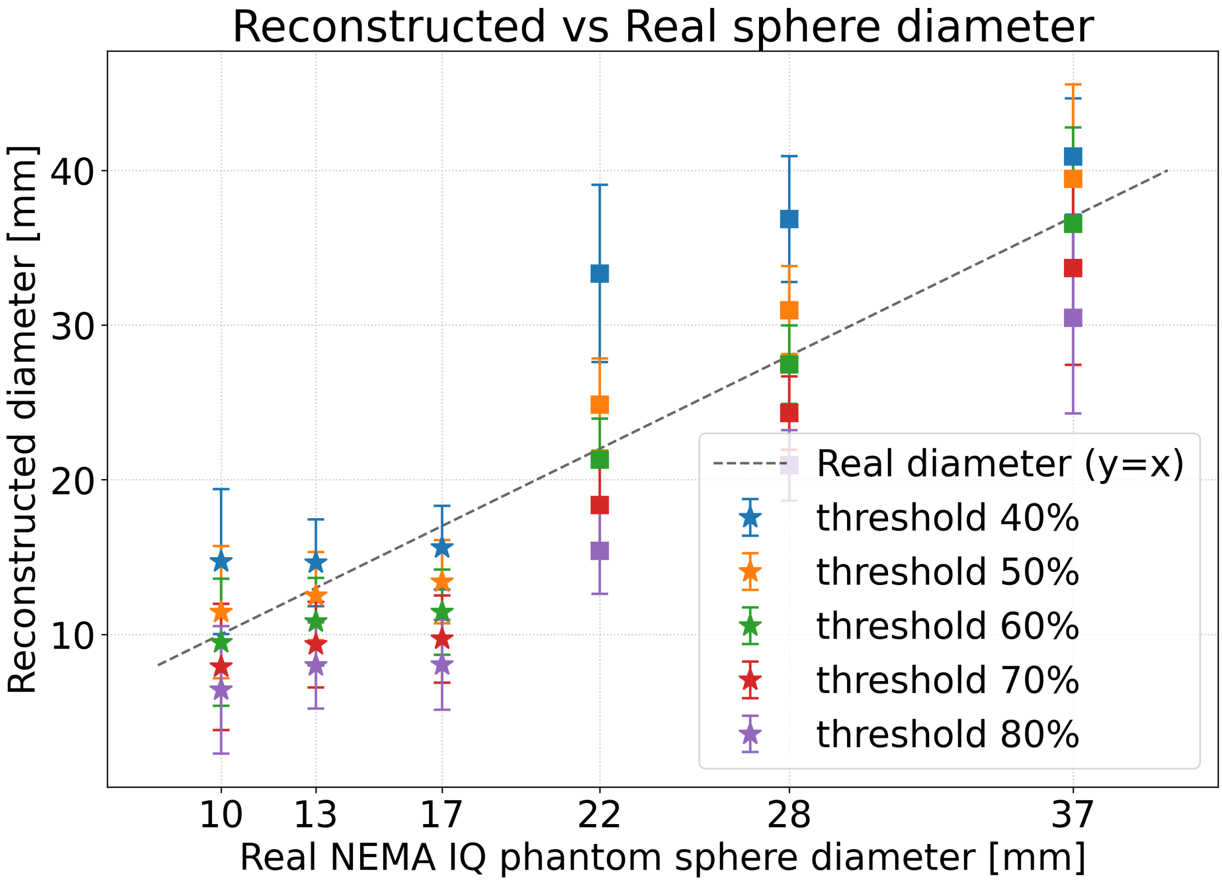

Figure 8: Reconstructed vs. real sphere diameter for experimental ^{18}F (spheres 10, 13, 17 mm) and ^{44}Sc (spheres 22, 28, 37 mm) data at intensity thresholds of 40%-80%. The dashed line indicates perfect reconstruction ($y = x$). Error bars represent uncertainties.

Appendix 4

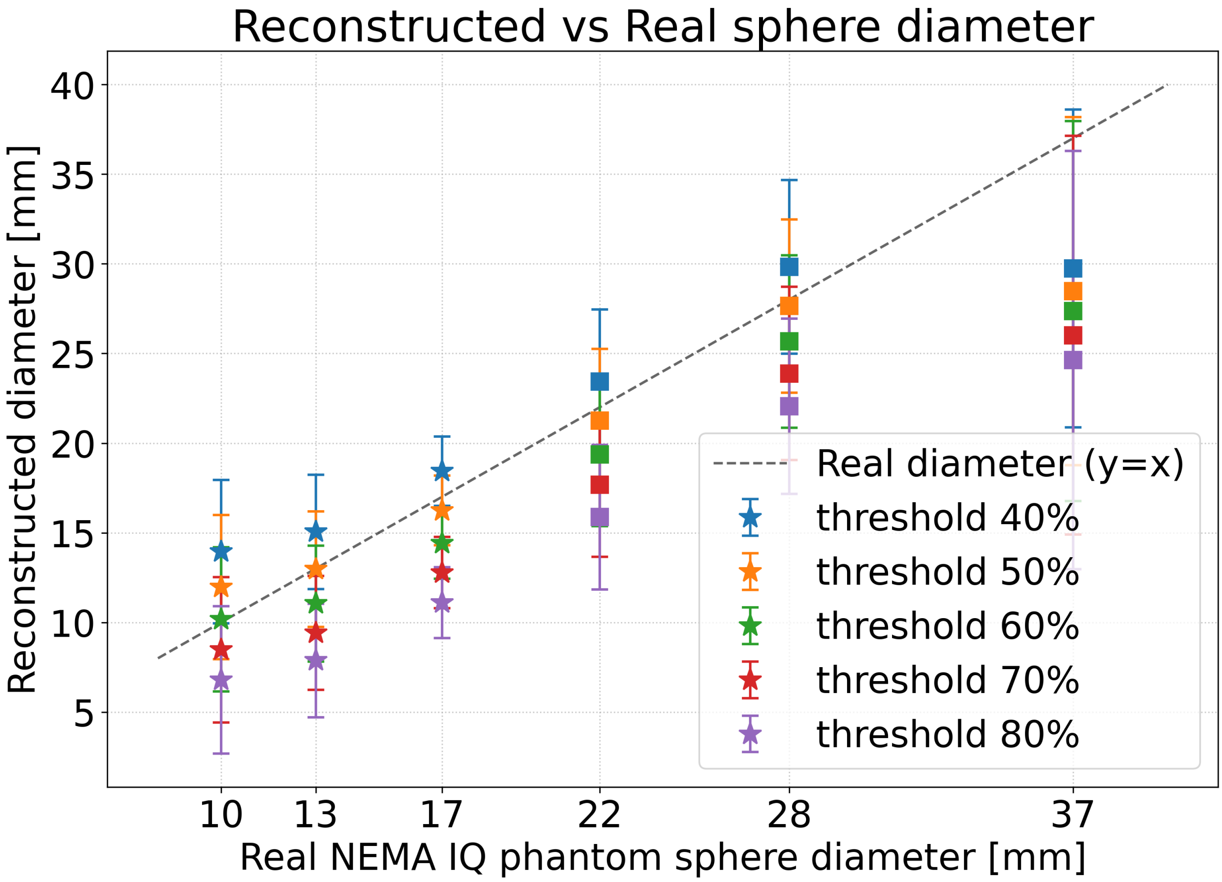

Figure 9: Reconstructed vs. real sphere diameter for simulated maximum range ^{18}F data at intensity thresholds of 40%-80%. The dashed line indicates perfect reconstruction ($y = x$). Error bars represent uncertainties.

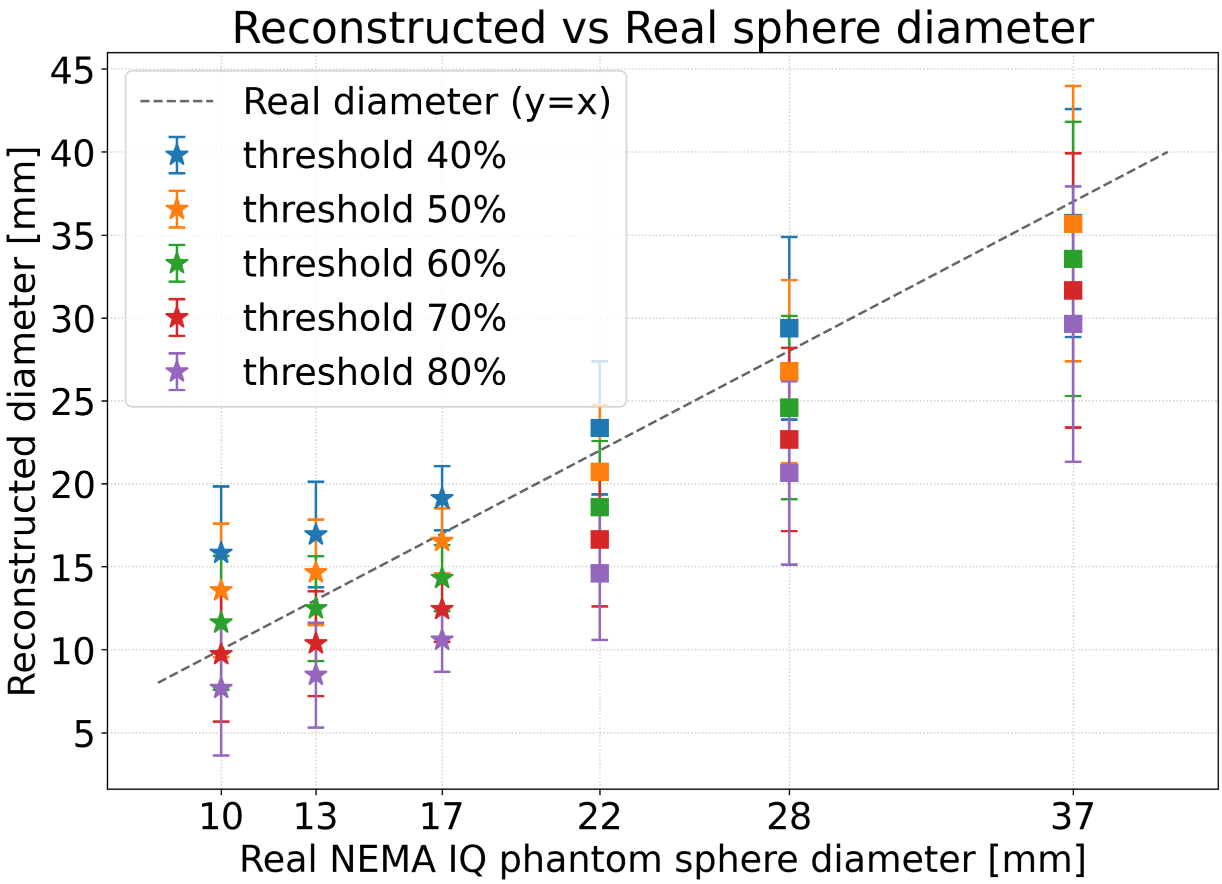

Figure 10: Reconstructed vs. real sphere diameter for simulated maximum range ^{44}Sc data at intensity thresholds of 40%-80%. The dashed line indicates perfect reconstruction ($y = x$). Error bars represent uncertainties.

Appendix 5

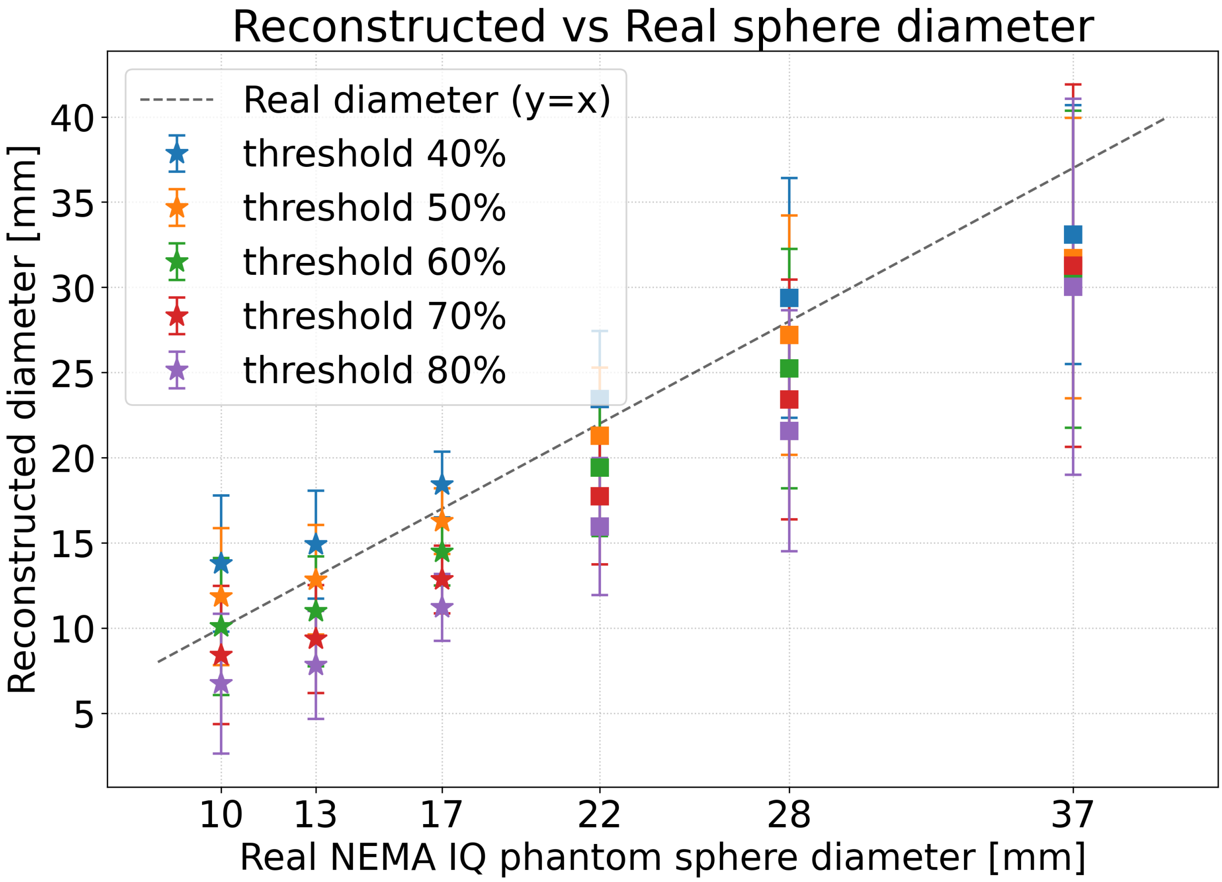

Figure 11: Reconstructed vs. real sphere diameter for simulated mean range ^{18}F data at intensity thresholds of 40%-80%. The dashed line indicates perfect reconstruction ($y = x$). Error bars represent uncertainties.

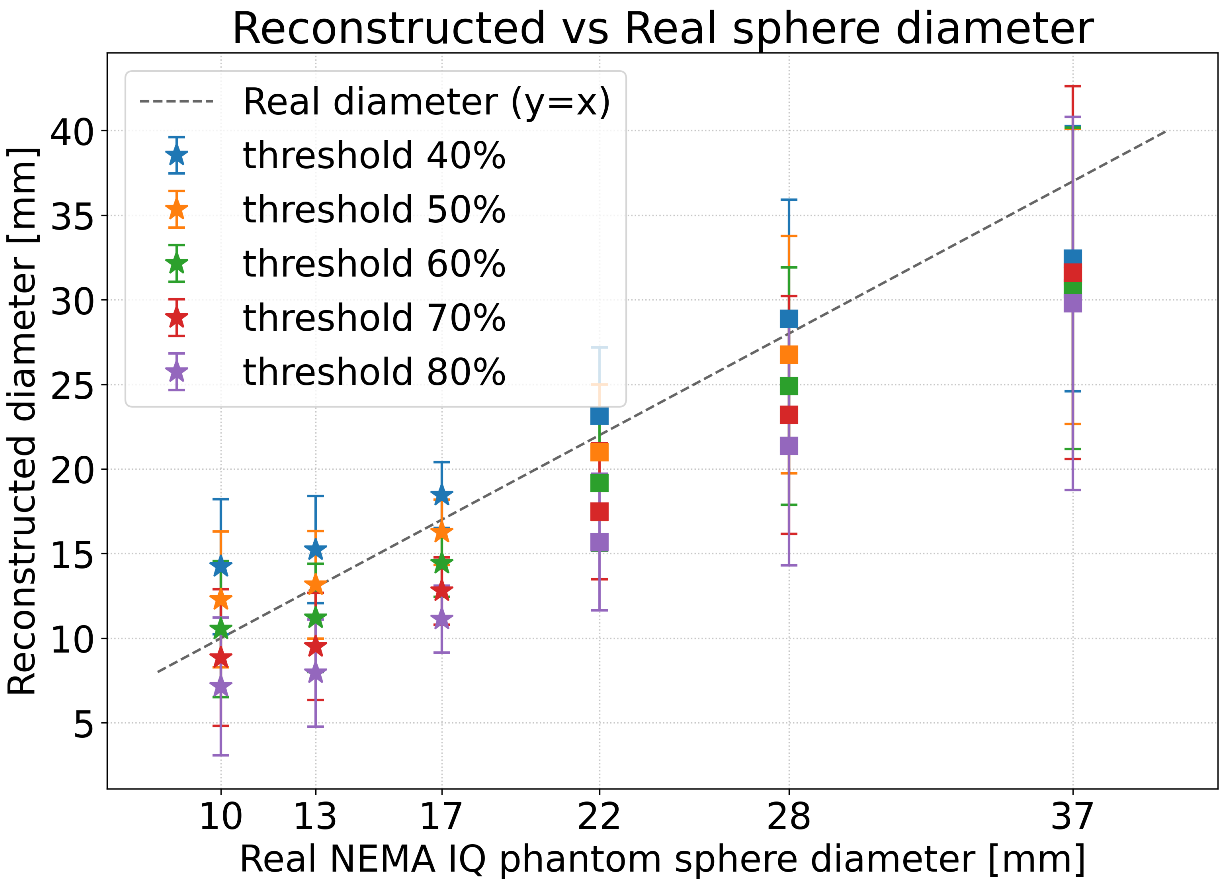

Figure 12: Reconstructed vs. real sphere diameter for simulated mean range [44]Sc data at intensity thresholds of 40%-80%. The dashed line indicates perfect reconstruction ($y = x$). Error bars represent uncertainties